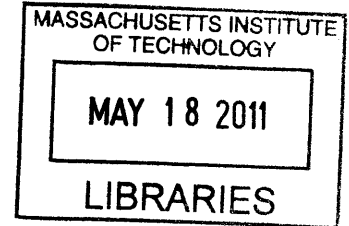# Design, Fabrication and Mechanical Optimization of Multi-Scale Anisotropic Feet for Terrestrial Locomotion

by

Jeffrey W. Morin

Sc.B. Mechanical Engineering
University of New Hampshire, 2009

Submitted to the Department of Mechanical Engineering
in Partial Fulfillment of the Requirements for the Degree of
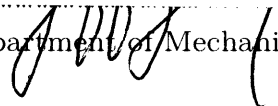Master of Science in Mechanical Engineering

at the
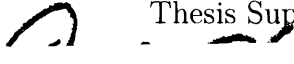
Massachusetts Institute of Technology

February 2011

Signature of Author..
Department of Mechanical Engineering
1st Dec. 2010

Certified by...
Anette E. Hosoi
Professor of Mechanical Engineering
Thesis Supervisor

Accepted by...
David E. Hardt
Professor of Mechanical Engineering
Graduate Officer

Design, Fabrication and Mechanical Optimization of Multi-Scale Anisotropic Feet for Terrestrial Locomotion

by

Jeffrey W. Morin

Submitted to the Department of Mechanical Engineering
on 1st Dec. 2010 in Partial Fulfillment of the
Requirements for the Degree of
Master of Science in Mechanical Engineering

ABSTRACT

Multi-scale surface interaction methods have been studied to achieve optimal locomotion over surface features of differing length scales. It has been shown that anisotropy is a convenient way of transferring an undirected force to a preferred direction or movement. In this thesis, the fundamentals of friction were studied to achieve a better understanding of how to design multi-scaled robotic feet that use anisotropy for terrestrial locomotion. Static and kinetic friction coefficients were found for novel test geometries under varying load conditions. The test geometries were manufactured with materials of variable durometer and were tested using unconventional rheometry methodology. Test results were then compared to standard friction laws. As predicted, the effects of contact area were shown to have an effect on the friction forces experienced by the softer materials. The contact area effects were then modeled as Hertzian contacts for a given material.

Verification of the area dependencies for the materials with adhesive effects was performed for the samples used in the friction tests. The samples were subjected to varying compressive force and images of the corresponding contact areas were obtained using an inverted microscope. The microscope images were then processed using MATLAB's image processing toolbox to find the actual contact area for the samples. The contact area results were shown to be in accordance with Herztian contact principles.

The effects of varying surface roughness were also studied for a given anisotropic arrangement of bristles. The array of bristles was used to provide propulsion to a controllable robot called BristleBot. The untethered nature of the robot allowed for unhindered velocity and force measurements that were used to analyze the effects of surface roughness. The force input for the robot was provided by two vibration motors that created an excitation which was then translated to horizontal movement by the anisotropic formation of the bristles. It was found that the BristleBot was able to achieve optimal locomotion when roughness conditions were minimized. Results of the anisotropic friction and adhesion tests were used to improve footpad development for soft robotic platforms.

Thesis Supervisor: Anette E. Hosoi
Title: Professor of Mechanical Engineering

ACKNOWLEDGEMENTS

I would like to express my gratitude towards all those who helped me along during my MIT experience. Professor Hosoi, you were consistently there for me with insightful words and never-ending wisdom that were always accompanied by an encouraging smile. Your passion and focus on your academic endeavors were major inspirations for me. Professor McKinley, you have also been great help in accelerating my academic mindset and helping me to grasp ideas that were sometimes out of my reach.

Team Peko helped me to get a real jump start with my immersion into the MIT culture and practices. Randy, you were a major help from the start by lending your expertise and experience to me without hesitation. Ahmed thank you for being such a great friend and helping me get through Fluids. Thomas and Johannes, your antics made daily lab life interesting and will live on in my thoughts. Nadia and Sarah, thank you for always being there when I needed any little thing and for making SQUISHBot fun. I appreciate Justin, Arvind, and Vivek for giving me their elder knowledge when I needed it most. Aditya, I'm not sure if you will ever know how much I appreciated our daily lunch talks. Our trip to India was epic! Again, major thanks for the fluids help you stud.

Throughout my life, my family has been there every step of the way. Mom and Dad, I am thankful for your guidance as parents as well as friends. Emily, thanks for being such a great sister... you are going to make it big someday! Scott, although you will always be my little brother, I still find myself constantly looking up to you. I can't wait to see all the great things you'll do later on in life. I hope you all know how much you mean to me and that I will always be there for you.

Crystal, I am so happy to have my best friend as the love of my life. Thank you for always giving me the best advice and for giving me a great life to look forward to. I am excited to start our next journey together doing the things we love!

CONTENTS

FIGURES

TABLES

1

INTRODUCTION

Contact mechanics take part in every aspect of the world around us. The way objects interact with one another influences everything from material properties to dynamic associations. Without contact mechanics, simple actions such as walking or picking up a pencil would be impossible. It's easy to see why studying contact mechanics is helpful in developing mobile robots; however, how should one choose the best type of contact for a specific application? To answer this question, the fundamentals behind the different types of contact must be studied.

Nature has been perfecting contact mechanics for millions of animals in environments all over the world. Throughout history, researchers have been attempting to mimic the different aspects of evolutionary locomotion. With each of these attempts, developers must decide on the types of interactions between their device and various surfaces. Surface-surface interactions for robotic locomotion can range from sub-micron-scale to macro-scale. Macro-scale interface interactions can usually be defined by fundamentals in mechanics while achieving sub-micron scale interactions usually involves molecular forces as the primary foundation for contact effects. Combinations of surface interaction mechanisms are typical in most biological systems that are successful in a variety of terrain types. These mechanisms are often combined in parallel or series to achieve adaptability over a wide range of surface types. One example of combined

surface interactions in nature can be seen in grasshoppers. Their legs allow then to walk and jump on large scale surface profiles while sticky pads on their feet allow for successful locomotion on surfaces that are inclined with varying roughness.

Within the topic of contact mechanics, coulomb friction is one of the primary principles. Typical examples from physics include boxes sliding down slopes or racecars going around turns, with the force of friction in each case determined by a material-based coefficient of friction and the applied normal force. While coefficients of friction in conjunction with normal force measurements can be helpful for predicting frictional forces, they do not tell you *how* or *why* the surfaces are interacting in such a manner. A closer look at the surface interface shows us that the frictional forces are determined by the mode in which the contact surfaces interact and to what degree the contact is made. Dispersive adhesion is one type of contact that involves the interaction of two materials through van der Waals forces. Adhesion can also take other forms such as mechanical adhesion (filling pores), chemical adhesion (atomic bonding), and electrostatic adhesion (electrical charge attraction) [1].

The role of contact interactions in mechanical devices can determine the effectiveness and efficiency of the overall design. The future of mechanical design looks towards the development of autonomous robots that interact with their surroundings in a natural and unobstructed manner. Robotic locomotion will play a critical role in minimizing human risk factors by substituting specialized robotic deployment into environments that are dangerous or inaccessible to humans. Current field robots underperform in field tests and typically last only 6-20 hours without incident according to a meta-study by Carlson and Murphy [2]. Unreliability is often caused by variable environments that have boundaries that are not in-line with a robot's operating range. As the world becomes more and more industrialized, the need for efficient machines and

13

actuators will proliferate the requirement for well-designed surface interactions and specialized contact designs.

1.1 Approach: Multi-scale Surface Interaction

Although there have been many developments in the field of robotic locomotion, there has been a lack of focus on the critical surface interactions that take place between the machines and their environments. Many robots have focused on different gaits of movement, attempting to mimic similar movements made by animals. The major two divisions of terrestrial transportation for animals fall into the categories of legged and limbless locomotion. While legged locomotion can provide tremendous landscape adaptability for a given length scale, its overall complexity requires greater development and effort to pursue. Limbless locomotion allows for superior stability, traction methods, and improved redundancy. Without protruding appendages, limbless robots also have improved sealing methods. Snake-like locomotion lends itself to improved functions in exploration, hazardous environments, inspection, and medical interventions. Limbless locomotion can be broken down into multiple modes that include two-anchor movement, rolling methods, and pedal locomotory waves. Other forms for limbless locomotion employed by highly successful snakes include lateral undulation, side-winding, and rectilinear locomotion.

The purpose of this thesis is to investigate and encourage development of multi-scale robotic surface interactions. Specifically, the proposed solution employs limbless motion methods incorporated with specialized material selection to improve multi-material contact success. In a world of miniaturized electronics and applications, a demand for smaller robots and propulsion methods has been on the rise. Traditional rotary and wheel-based movement methods do not meet the physical demand of such small-scale endeavors

due to motor, friction, and contact constraints. There have been many robots that have successfully achieved limbless locomotion such as Carnegie Mellon's serpentine based robot [3]; however, these robots require modifications to achieve optimal locomotion over a given surface.
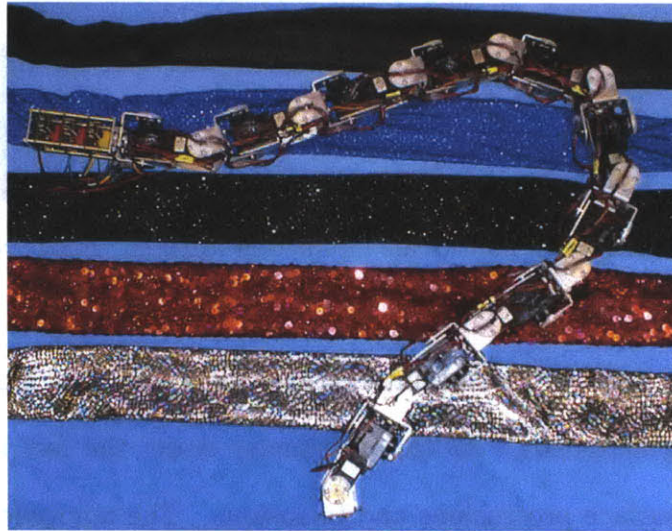
Figure 1: Snake robot with additional skins to match a variety of surface treatments. Image reproduced from [3].

To achieve successful contact interactions over a wide variety of surfaces, a wide variety of contact techniques must be used. The proposed approach to achieve locomotion over a diverse range of surface structures involves utilizing contact mechanics principles with differing surface interaction scales. A biomimetic example of such technique can be seen in Sangbae Kim's Stickybot [4].

Figure 2: StickyBot's foot with multi-scale interaction features. Image reproduced from [4].

At the largest scale of surface interaction, the gecko has highly compliant limbs that are moved using actuators. At the centimeter scale, the feet are divided into toes that can conform to surface protrusions and inclusions. The micrometer scale interactions are handled with setae that are located on the bottom of the toes. The tips of the setae are further divided into spatula that can interact with surface geometries at the <500 nanometer scale [4].

To achieve successful locomotion over varying surface forms, a combination of interaction modes will be used including friction, adhesion, and mechanical interactions. The shape, size, and mechanical interaction methods used for locomotion determine the range over which an appendage can be effective for transmitting movement force over a surface. The hierarchy of physical interactions with features of varying scales will be used to successfully interact with the relevant length scales of variable surface environments. The physical constraints for each type of contact interaction method will be matched with geometry specifications that will provide for the most effective contact methods.

1.2 SQUISHbot: A Soft Robot with Soft Feet

The inspiration for the work presented in this thesis was generated by a DARPA program initiative geared towards creating "a new class of soft, flexible, meso-scale mobile objects that can identify and maneuver through openings smaller than their dimensions and perform various tasks." MIT's project team was based on a project called SQUISHbot and collaborated with researchers from Boston Dynamics. The project leaders for MIT consisted of Professor Martin Culpepper, Anette Hosoi, Dr. Karl Iagnemma, and Professor Gareth McKinley. Boston Dynamic's efforts were led by Robert Playter, who was co-PI of the project with Anette Hosoi.

Figure 3: SQUISHbot with active-fluid joints. String is attached to the spooler motor.

The DARPA ChemBot program required each team to work towards a unified set of goals to be met by a "soft" robot. The objectives set for the ChemBot included:

    a.) Travel a distance of 5 meters with a velocity of 0.25meters/minute

    b.) Achieve a 10-fold reduction in its largest dimension

c.) Traverse through a 1cm opening and reconstitute its original shape in 15 seconds [5].

Figure 4 shows SQUISHbot traversing through a 1.7cm hole using its prismatic joint and anisotropic footpads.

Figure 4: SQUISHbot traversing through hole using its prismatic joint & anisotropic footpads.

Additional capabilities for each robot such as carrying additional payloads were considered to be advantageous [5]. At the time this thesis was written, MIT's SQUISHbot team had achieved:

1. Crawling through a 1.75cm hole

2. Crawling at 17.5 mm/sec

3. Turning while crawling

4. Crawling on various surfaces including slate, concrete, fiberglass, rubber, and aluminum.

5. Climbing a 16 degree incline.

Throughout the SQUISHbot's design and manufacturing process, it was well known that the robot's surface interactions would be crucial in achieving many of the required tasks. To maintain a compact profile, a prismatic joint comprised of a 3D printed "designer" foam was used in force translation.
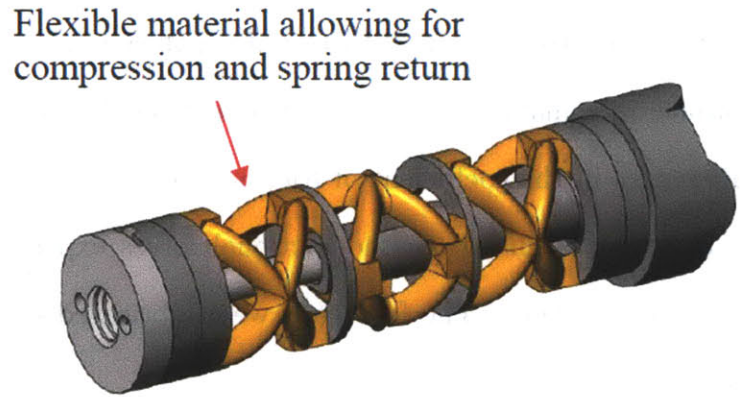
Figure 5: Prismatic joint for inchworm gait.

The actuation created by a spooler motor was combined with an anisotropic foot design. A stiff, slippery material was used on one side of the foot pad while on the other side a flexible, high-friction material was used. The foot pad had a connection neck that allowed the pad to rotate depending on the direction of the actuation. A 3:1 friction coefficient ratio was achieved with the footpad. The materials and mechanical action used in the foot pads will be further described in this thesis. The robot also employed active fluids which were utilized in turning and payload-carrying operations. Solder-locking joints were used to create a directional preference in the robot which could be activated by simply heating the joints with heated wires.

1.3 Specialized Contact Mechanics in Robotics

With project SQUISHbot as the driving force for development of new robotic locomotion methods, anisotropic friction and material specialization were selected as a focal point of robot-surface interactions. SQUISHbot utilized low-profile foot pads that combined a mechanical ratcheting action with a multi-material geometry that contacted the traversed the surface in a manner that was dependent on the direction of the robot's movement. The differences in the coefficient of friction between the two materials on the footpads were used to induce a change in the frictional forces experienced by the robot, thus creating unidirectional motion. The foot pads were fabricated using the 3D printing methods described in section 3.1.

There were many benefits to utilizing the 3D printer for the foot fabrication process. The Objet printer allowed for multi-material printing methods that incorporated materials with differing coefficients of friction into the models. To obtain fine normal force and frictional force measurements, a rheometer was used unconventionally by attaching the 3D printed foot pads to the rheometer measurement fixtures. The rheometer allowed us to obtain normal and tangential force measurements and also allowed us to apply constant forces over the testing area. The rapid prototyping methods also allowed for feet to be printed in an easy-to-test manner that was suitable for analysis in the rheometer. Since the rheometer used circular plates, the footpads were printed in a circular pattern that could be fitted to a flat geometry. The frictional forces experienced by the footpads in the circular pattern moving in a circular path translated to the same frictional forces that would be experienced for a linear path for a given applied normal force. The rheometer allowed for variation in applied normal forces while moving the samples at a given velocity. The low-profile (<1cm) requirement for the footpads was met by the 3D printer's ability to print scaled-geometries that were created in

SolidWorks. The printer's versatile material selection also allowed us to make changes in the flexibility at the rotational "neck" of the pads by selecting materials with different elastic modulus values. Figure 6 shows an example of the anisotropic footpads used on SQUISHbot.
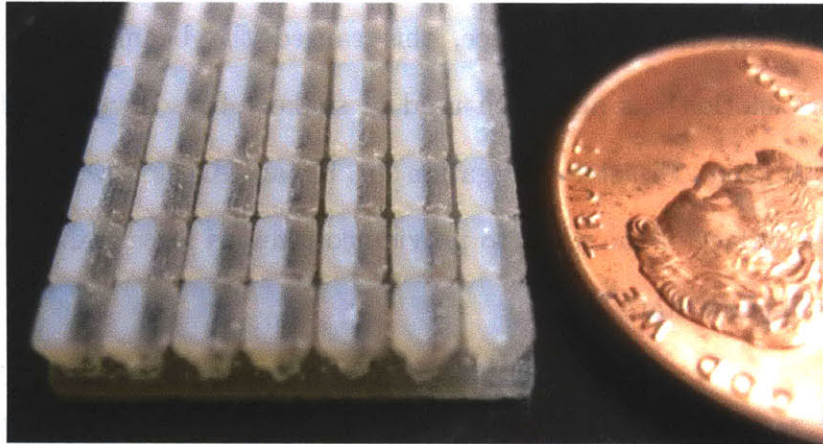
Figure 6: Actual anisotropic footpads used on the SQUISHbot robot.

For future robotic applications, the anisotropic properties and multi-material and directionally dependent geometries may be tuned for specific environments. Vibrational inputs have been shown to be a successful method of exciting directionally dependent geometries. For ciliary motion, vibrations that travel along thin, flexible beams can create directionally dependent forces that are based on the beam properties. These beams, which are sometimes called bristles, are used to translate the vibrational motion into propulsion by interacting with surface geometries. As the vibrations cause the bristles or traveling body to bounce up and down, bristles situated with a directional preference create an anisotropy that results in a net driving force for forward motion. Depending on the application at hand, the bristles can be tuned to meet the needs of varying surface geometries, through varying bristle length, thickness, and material selection. Bristle geometries can also be modified further with bristle-tip modification to

insure that the interacting surface-bristle materials achieve the optimal locomotion result. There have been a few projects that have employed ciliary motion as a core method in creating a driving force. One example for ciliary movement can be seen with linear actuators developed by Okinawa National College of Technology, which utilized bristles on either side of an actuated beam. As the forces translated from the bristles to the center beam with directional preference, this caused the beam to move in a chosen direction. Ciliary motion has also been used in snake robots developed for the "Special Project for Earthquake Disaster Mitigation in Urban Areas", which utilized bristles around the entire surface of the robot to provide continuous force translation regardless of the robot's rotated-plane state [6].
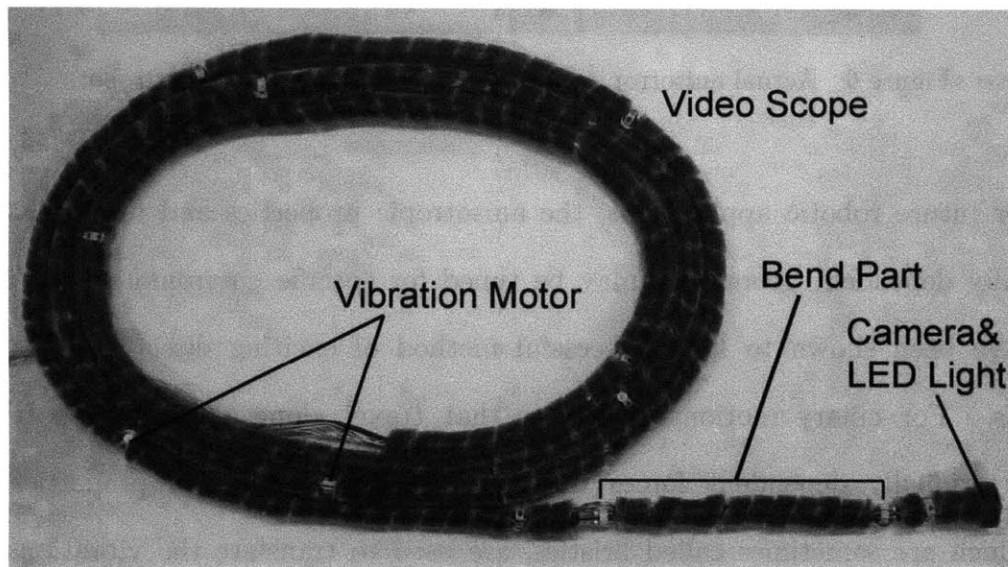
Figure 7: Active flexible cable driven by ciliary vibration mechanism. Image reproduced from [6].

2

CONTACT MECHANICS FOR ANISOTROPY

Successful force transmission between the robot and its contact surfaces is a critical function needed to achieve multi-scale terrestrial locomotion. Anisotropic mechanisms can be used to convert undirected force inputs into focused desired output. Desired outputs can be manipulated through material and mechanical design selection optimized for specific conditions. In this chapter, the fundamentals of friction and adhesion mechanics are studied to insure optimal anisotropic feet functionality.

2.1 Coulomb Friction

As previously mentioned, friction plays a major role in all forms of terrestrial movement. Without friction, there would be no traction between interacting objects, hindering any attempt of lateral movement. Depending on the scale of the interfacial interaction, the effects and physics behind friction can vary greatly. Typically, the basic properties of friction can be broken down into three laws: Amontons' 1st law, Amontons' 2nd law, and coulomb's law of friction. The fundamental concepts behind the Amonton's first and second law are that the force of friction is directly proportional to the applied load:

$$F_n = \mu N \qquad (1)$$

The force of friction is independent of the apparent area of contact, respectively [7]. Here, F_n is the experienced frictional force, μ is the coefficient of friction, and N is the applied. Equation (1) states that there is a coefficient of friction that directly relates the experienced frictional force to the applied normal force, regardless contact area. The reasoning behind this phenomenon is that the area of real atomic contact between two surfaces is usually proportional to the load. It should also be noted that the coefficient of friction is typically independent of velocity, except under circumstances where the sliding velocity is very low and thermal activation energies come into play [8].

2.1.1 Static vs. Kinetic Friction

With most material interactions there are two values given for the coefficient of friction: static and kinetic coefficients of friction. The static coefficient of friction is related to the amount of tangential force applied to a stationary object with a surface in contact with another stationary surface. As more and more force is applied to the object, eventually it breaks free and experiences sliding motion. Once the object is sliding, a force is still required to keep the object sliding. This force required for sliding is related to the kinetic coefficient of friction. Typically, the static coefficient of friction has a higher value than the kinetic coefficient of friction. Figure 8 shows the different coefficient regimes [9]:
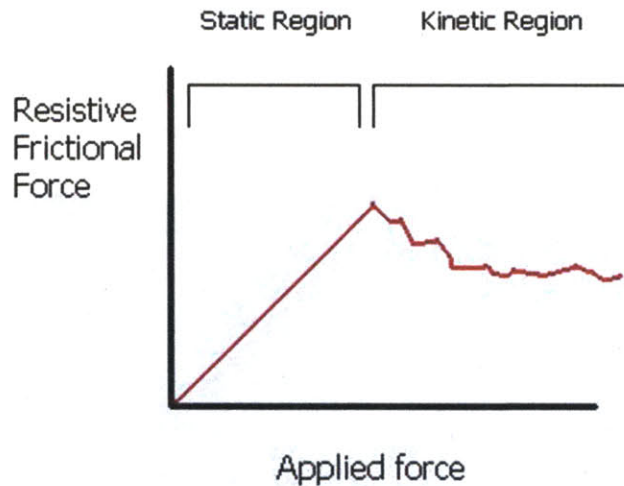
Figure 8: Different coefficient regiemes for varing frictional forces given an applied load. Image reproduced from [9].

It should be noted that there is a transition between static and kinetic friction where stick-slip motion may occur. The amount of time that an object remains in the stick-slip regime is dependent on the velocity of the object. During the stick-slip regime, there are often spikes in the coefficient of friction associated with a transition between static and kinetic friction. Stick-slip is often the cause of material "chattering" and can be harmful to precision devices such as bearings.

2.1.2 Area Independence

While it may seem counterintuitive, frictional forces between solid bodies are considered area independent. The reasoning behind this is that as the contact area increases, the pressure between the two surfaces for a given force is decreased. The increased frictional effects of a larger contact area are counteracted by the reduction of pressure. Since pressure is defined as a force divided by the area of contact, the resulting

frictional forces are dependent only on the frictional coefficient and the applied normal force.

Figure 9: A scale pulling a plank demonstrates that frictional force is approximately contact area independent. Image reproduced from [10].

It should be noted that it is not well understood why the force of friction resulting from nano or micro-scale asperity contacts depends on the applied normal force. Such contact scales require in-depth comprehension of the complex frictional behavior between the fundamental mechanisms underlying the atomic interactions [11].

2.1.3 Material Flipping

For the SQUISHbot project, differences in material coefficients were exploited for the robot's 3D printed feet. The two different types of materials used on the footpads had very different coefficients of frictions. Anisotropic behavior was achieved through flexible "stalks" that allowed the robot to experience low friction conditions while moving forward and high friction conditions when the spooler motor recoils. The design had two main features, a low-durometer polymeric material and a "finger nail" like structure that

was a hard polymeric material. As illustrated in Figure 10, switching the surface of the "toe" in contact with the traversing surface from a hard to soft allows for a transition of motion from sliding to sticking.

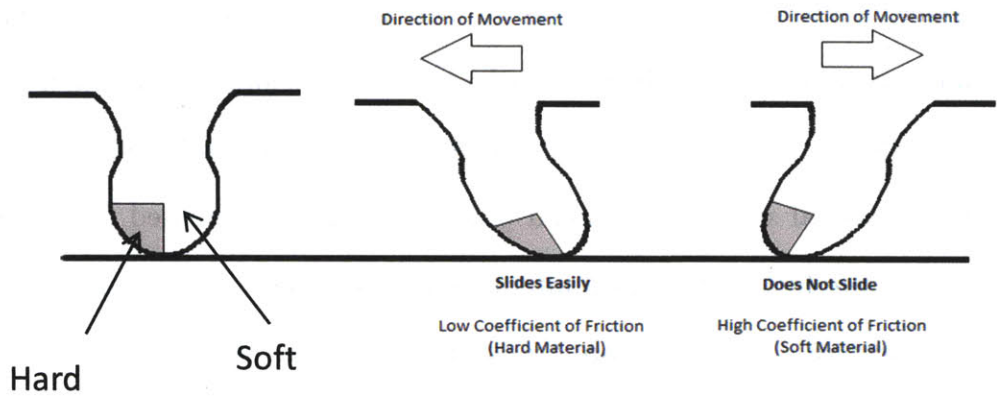Figure 10: Illustration of material flipping mechanism used to create anisotropic feet for SQUISHbot.

Figure 11 shows the actual foot pad design used on SQUISHbot. The soft material was made of TangoPlus while the hard material was made of TangoWhite (material properties can be seen in section 3.1).
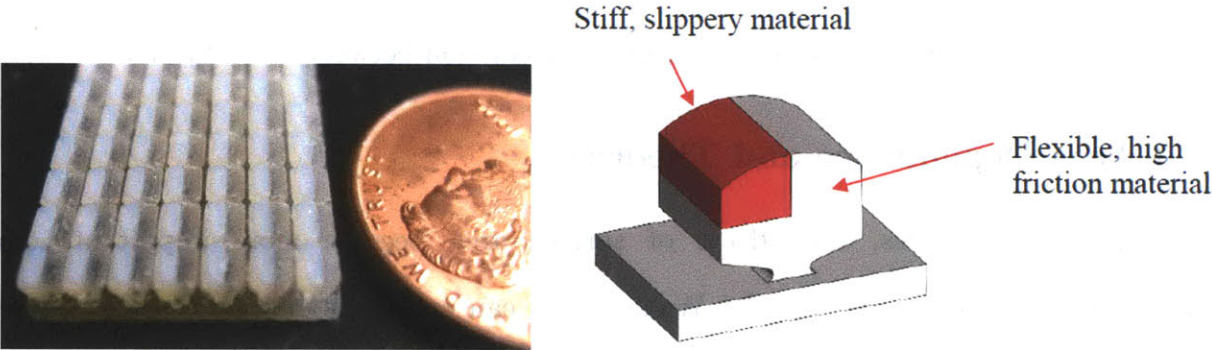
Figure 11: (L): Photo footpads used on SQUISHbot (R): Breakdown of 3D model for a single pad.

2.2 Adhesion

In general, soft solids have greater friction than hard solids when in contact with the same surface. Soft substrates, such as rubber, have surfaces that are compliant to inclusions and protrusions which allows for a larger area of contact. Adhesion is typically used to describe the attraction between two dissimilar materials while cohesion is the term used for similar material species. It should be noted that the increased friction for softer materials is not a product of jamming interactions but rather the van der Waals forces between the molecules that make up the surfaces. This has been demonstrated in experiments by Chaudhury and Whitesides, where the effects of adhesion on vertically lifted hemispherical contacts have been studied [12]. Surface energy can be used to relate a material's adhesive properties, which fall in a variety of categories ranging from chemical, dispersive, and diffusive adhesion, to its surface area. The work per surface area required to separate two adhered materials is dependent on the work to break each bond. Due to the related bond energies, adhesive hysteresis is often a characteristic displayed as a result of time-dependent bond formations and restructuring [13]. Adhesive properties are typically used when it is desired to "stick" one object to another, as in the case with tape or stickers but can also be used for force transmission between two objects.

2.2.1 Area Dependence and Theories

At smaller scales, the effects of surface area become more important. As mentioned before, attractive van der Waals forces can create a temporary bond between molecules of two surfaces in contact. Soft materials such as rubber or PDMS increase the effects of the surface interactions. Depending on the mode of contact, equations have been developed to calculate the contact area of a hemisphere given an applied force. The

effective contact modulus can be calculated using the elastic modulus and Poisson's ratio of each surface material [14].

$$\frac{1}{E_c} = \frac{1-v_1^2}{E_1} + \frac{1-v_2^2}{E_2} \tag{2}$$

Where v_1 and v_1 are Poisson's ratio for each material, E_1 and E_2 are the elastic modulus for each material, and E_c is the overall effect contact modulus. The effective radius for the two materials used in the Hertzian contact and JKR equations can be calculated as follows [15]:

$$\frac{1}{R_c} = \frac{1}{R_1} + \frac{1}{R_2} \tag{3}$$

Where R_1 is the radius of the tested hemispherical samples described in section 3.1, R_2 is the surface to which the hemispheres were applied, and R_C is the effective radius. For the flat base surface, R_2 was said to have an infinitely large radius, therefore $1/R_2 = 0$.
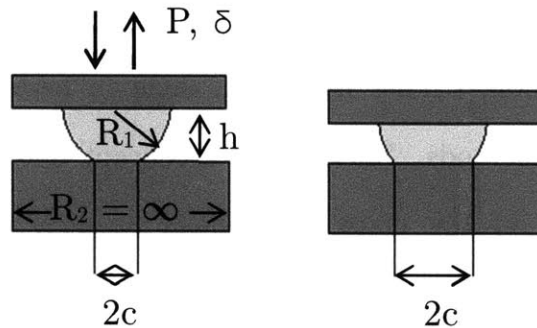
Figure 12: Hemispherical sample layout.

Using the Hertzian contact rule, the radius of contact (c) can then be calculated using the applied normal force, the effective radius of curvature, and the effective elastic modulus [15].

29

$$c = \left(\frac{3NR_c}{4E_c}\right)^{\frac{1}{3}} \tag{4}$$

Where N is the applied normal force. When the adhesion comes into play, the attractive forces (contact energy) give way to the expression derived by Johnson, Kendall, and Roberts [16]. Their equation takes into account the effects of the energy release rate (G) between the two substrates:

$$c^3 = \frac{3R_c}{4E_c}\left(N + 3\pi GR_c + (6\pi GR_c N + (3\pi GR_c)^2)^{1/2}\right) \tag{5}$$

Where G is defined as the energy release rate. The highlighted region represents the supplementary effects of adhesion in addition to the Hertzian contact.

2.2.1.1 Tests by Others

With many biological locomotion methods dependent on adhesion for tangential loading and force transmission, studies have been done to better capture the effects of dissipation in such contact methods. Stickiness is a concept that has eluded scientists for many years, often because of the many mechanical nuances that occur between the interacting substances. Heterogeneities in a material are often be thought of as performance weak spots; however the dissipative mechanisms in the substance can give rise to extra adhesive energy in the bulk or at the interface. This can be seen in the nonlinear traction curves as measured by Gent and his coworkers working with adhesive joints [17].
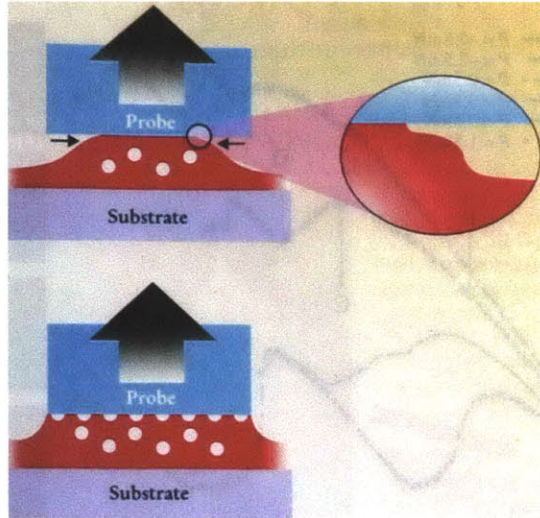
Figure 13: Cavitation in thin films subjected to normal pulling off. Image reproduced from [17].

Waters and Guduru performed experiments on polydimethylsiloxane (PDMS) samples and took measurements of contact area during mixed normal/tangential loading conditions. They found that the strong dependence of the work of adhesion upon mode mixity can be captured effectively by a phenomenological model in the regime where the contact area stayed circular and the slip was negligible. They also noted rate effects that were described by a power-law dependence upon the crack front velocity [18].
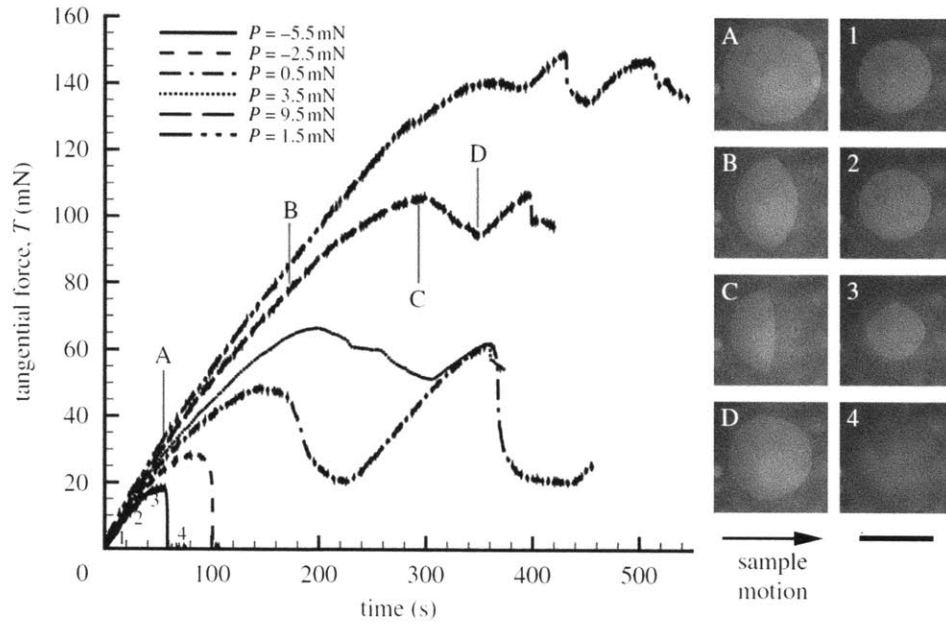
Figure 14: Water's experimental data for tangential force vs. time at various constant normal loads. Image reproduced from [18].

Chaudhury and Whitesides also looked at the direct measurement of interfacial interactions between semispherical lenses of PDMS [12]. Both groups found a strong correlation between the JKR theory and their deformation results. Figure **15** shows the setup used in Chaudhury's compression tests and a corresponding test image.
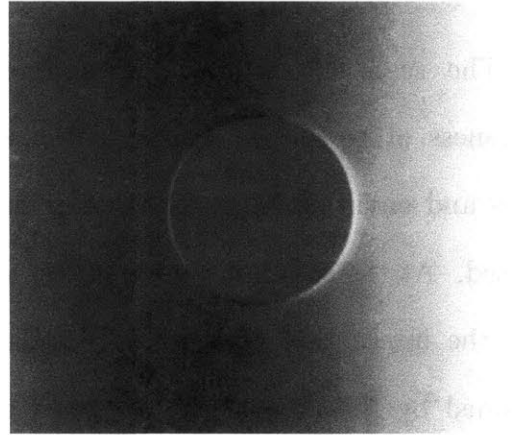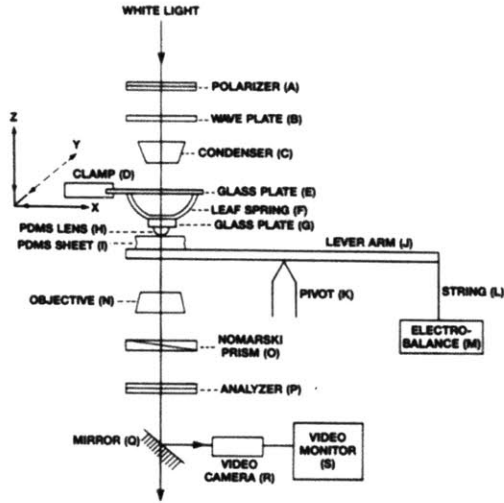
Figure 15: (Left) Setup description for Chaudhury's compression tests (Right) Image of PDMS compression. Image reproduced from [12].

For tangential loading, the bonds formed by adhesion also have an effect on the experienced frictional force. The tangential stress that can be withstood by these bonds is known as the adhesive shear strength (S) and relates frictional force to the area of contact (A) [21]:

$$\mathbf{F_n = SA} \tag{6}$$

This equation largely applies to rubbery materials, where their high compliance allows them to have a large contact area with an opposing surface. Forearm skin is one example that was shown to exhibit a similar relation. Experiments performed by Koudine and Barquins showed that the coefficient of friction for the forearm skin was related to factors that included Hertzian contact and elastic modulus dependence [22].

2.3 Multi-scale Terrestrial Methods

The scale of surface-body interactions plays a major role in determining the effectiveness of rectilinear motion. For robots that are required to transverse varying surfaces and environments, the issue of dealing with multi-scale contact physics must be addressed. At the smallest length scales, attractive van der Waals forces can play a major role in the interaction between two surfaces. The magnitude of the attractive force is determined by the area of contact between the two surfaces. As the surface roughness length scales increase, significance of the van der Waals attraction decreases and the effect of mechanical interactions becomes more prominent. Depending on the direction of motion, fibers laid with a directional preference to produce anisotropy can exhibit differing resistive effects. This is because the buckling parameters change for the fibers as a function of load direction, thus changing the force required for the fibers to move from one surface inclusion to the next. By changing the length and diameters of the fibers, the buckling effects can also be modified to fit a specific terrain scale. Combining the effects of adhesion and mechanical buckling parameters allows for the possibility of a wide variety of terrain scales to be traversed. Once the scale of surface geometries is larger than the characteristic scale of microstructural arrays, macro structures must be employed to make optimal contact with the surface profile. Large-scale surface interactions are usually on a similar order of magnitude as the traversing body.

2.3.1 Examples in Nature and Science

Most animals display some degree of multi-scale adaptation for mobility. Humans, for example have arms and legs on the largest scale of surface interactions, fingers and toes on the next scale, and finally skin and hairs on the smallest interaction scale. House

34

cats also utilize a number of physical mechanisms for increased mobility. The cats have feet that include deformable footpads for traveling on level ground. For sloped or rough terrains, the cats can also deploy claws with a variety of orientations. The footprint of a lizard toe with a smooth substrate can be shown to have many scales of contact. As seen in Figure 1, the longest length scale is ~10 mm^2 between the lizard toe and the substrate. The lizard skin then has long fibers or hair known as setae which then have smaller fibers on top of then. The larger hairs have a length of ~200 µm and a radius ~3 µm while the 1000's of smaller hairs on each long fiber has a length of ~20 µm and a radius of ~.1 µm [23].
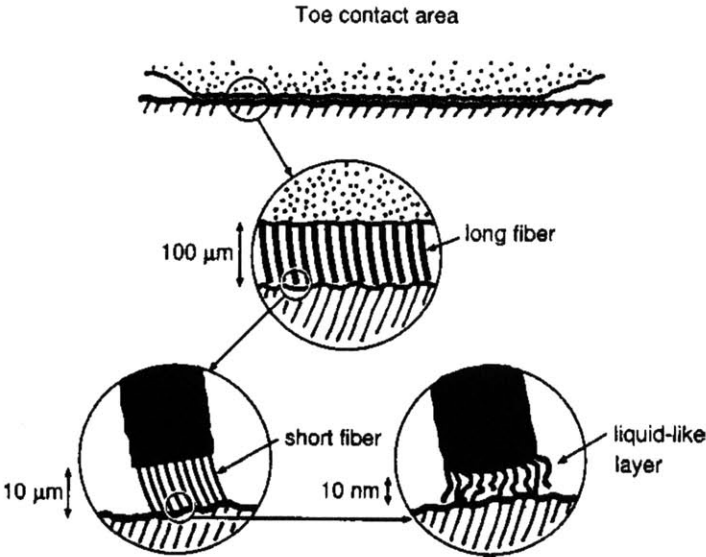
Figure 16: The many scales of contact between a lizard toe and a smooth substrate. Image reproduced from [23].

Spiders and other insects also exhibit varying ranges of contact scales and have been used as a basis for bio-imitation robots. One example can be seen in Sameoto and Menon's multi-scale compliant foot designs for use with a spider-inspired climbing robot [24]. The robot employed macro, micro, and nano-structural design for the robot legs and

feet to achieve a greater range of mobility for space applications. Integration of multiple types of contact methods improves the odds of successful contact over a greater variety of surface types.
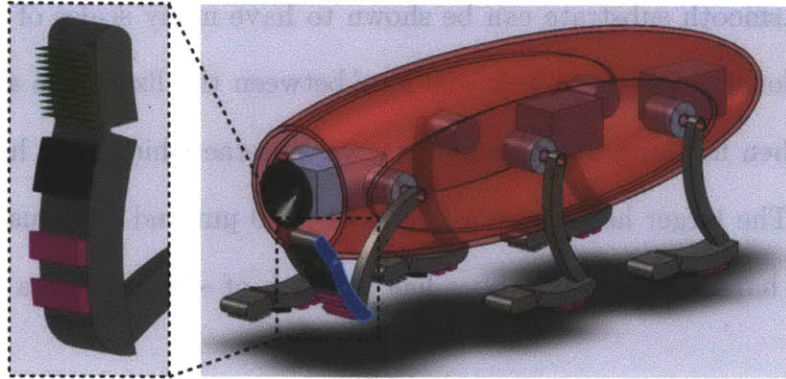
Figure 17: Sketch of integrated concept.

Advancements in fabrication techniques have made it easier to produce multiscaled features composed of multiple materials. Spinybot is a robotic example employing multiple modes of traction methods, much like the house cat. The spines used on the robot were primarily a function of the surfaces to be climbed, and not of the robot size. Because of this, heavier robots using a similar spine structure would require more spines per foot [25]. Figure 18 shows various microstructures that have been fabricated in attempts at bio-imitation to achieve adhesion, traction, and climbing.
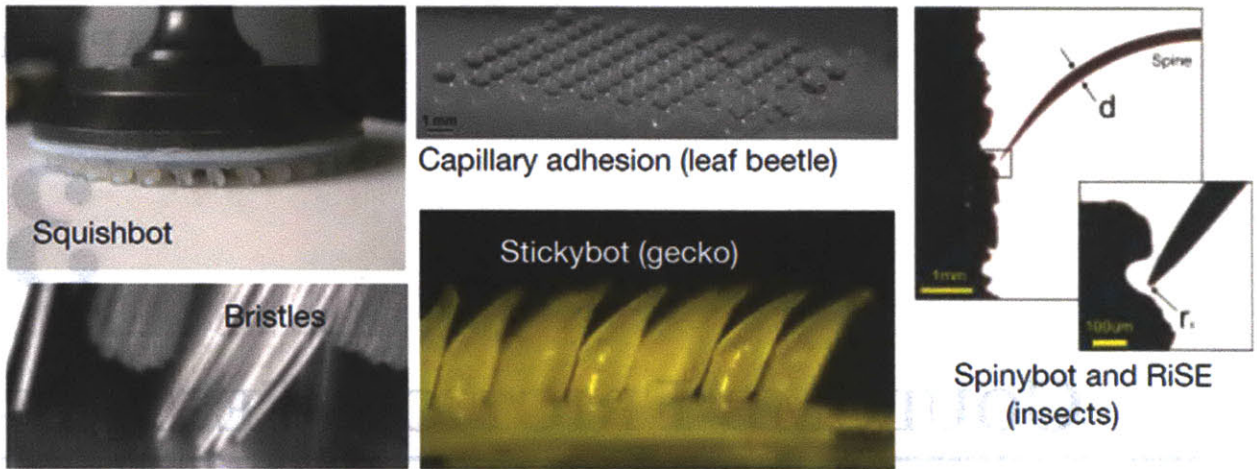
Figure 18: Various microstructures that enable adhesion, traction and climbing.

3

COULOMB FRICTION TESTING

Testing procedures were used to verify fundamental friction principles for a variety of rapid prototyped materials and structures. Force input and output readings for the samples were obtained through unconvential used of rheometry devices in order to achieve accurate data. The fundamental contact mechanics described in chapter two were compared to measured data. Proof-of-concept tests were conducted with the tested materials to prove the viability of the anisotropic contact designs.

3.1 Materials

Rheometer tests were performed to find the material properties of the 3D printed materials as well as to observe the effects of the sample shape on friction results. The rheometer used in the tests was a Texas Instruments AR-G2. The standard 'AR Instrument Control' panel was used for device input through a Dell Optiplex GX270. A standard 40 mm diameter flat aluminum geometry was used with the printed samples so that the applied forces would be evenly distributed. Prior to the tests, the rheometer was calibrated for geometry and instrument inertial changes. Rotational mapping was also performed to achieve better accuracy for low torque ranges. The base plate for the rheometer was coated with a standard chromium material and was wiped clean prior to use with ethanol and Kimwipes. The heater coils or peltier plate were not used during

throughout the tests. The rheometer height was zeroed prior to loading the samples onto the geometry due to the compressibility of the samples. Normal forces applied to the samples were maintained through the automatic calibration system in the rheometry software. Due to the auto-regulation of the applied normal forces by the rheometer, screen shots of the instrument status screen were used to obtain real-time normal force measurements experienced by the samples, regardless of the set normal force input.

Table 1 shows some of the rheometer specifications:

Table 1: TI AR-G2 Specifications

Machine Property	Value	Units
Maximum Torque	200	mN.m
Torque Resolution	0.1	nN.m
Angular Velocity Range	0-300	rad/s
Displacement Resolution	25	nrad
Axial Force Range	0.005-30	N

To create the 3D printed samples, SolidWorks 2009 was used. The sample assembly files were created in the standard part file format and then converted to two STL files, each of which represented all of the features of one material. By saving all features of the same material as one part, it simplified the STL loading and configuration process for the Objet printer interface. Material printing properties were limited to the technical specifications of the Connex500 3D printer. Table 2 shows the technical specification for the 3D printer in the X, Y, and Z build resolutions along with the printers build layer and accuracy rates.

Table 2: Connex500 Technical Specifications

Layer Thickness (Z-axis)	Value	Units
Horizontal build layer size	16	microns
Build Resolution		
X-axis	600	dpi
Y-axis	600	dpi
Z-axis	1600	dpi
Accuracy		
(Dependent on orientation/size)	0.004 - 0.01	inch

The Objet printer is capable of printing a variety of materials. Table 3 shows the general material properties for the three main types of materials used in the tests. FullCure720 and VeroWhite were used for their high elastic modulus and support capabilities while the TangoPlus was used for softer and "stickier" elements.

Table 3: Connex500 Material Properties and Specificaitons

Property	ASTM[1]	Value	Units
FullCure720			
Tensile Strength	D-638-03	60	Mpa
Modulus of Elasticity	D-638-04	2870	MPa
Elongation at Break	D-790-03	20	%
VeroWhite - FullCure830			
Tensile Strength	D-638-03	50	Mpa
Modulus of Elasticity	D-638-04	2495	MPa
Elongation at Break	D-790-03	20	%
TangoPlus - FullCure930			
Tensile Strength at Break	D-412	1.5	Mpa
Modulus of Elasticity ($\varepsilon = 0.20$)	D-413	0.1	MPa
Modulus of Elasticity ($\varepsilon = 0.30$)	D-414	0.2	MPa
Modulus of Elasticity ($\varepsilon = 0.50$)	D-415	0.3	Mpa
Elongation at Break	D-412	218	%
Tensile Tear Resistance	D-624	3	Kg/cm

The 3D printed samples consisted of a 40mm flat disk with 10 hemispheres equally spaced 13.5mm from the center. The hemispheres had a diameter of 2mm. To give the samples support, a 1mm layer of FullCure720 was used as a base upon which the hemisphere layer was applied. The hemisphere layer consisted of a 1mm base made of Tangoplus or Fullcure720, depending on the test. A hemispherical shape was chosen for the samples because hemispheres were a common geometry in past friction-based experiments and also simplified Hertzian contact analysis for the adhesion tests described in section 4. Double-sided 3M adhesive was applied evenly to the back of each sample and any excess adhesive

---

[1]ASTM = Standard of American Society for Testing and Materials

was trimmed. Each sample was centered on the plate so that even torques could be applied and measured. The rheometer peltier plate was used as the contact surface. The peltier plate was made of hardened chrome with a smooth finish.

3.2 Tests

There were three tests that were performed to determine fundamental properties for the materials with a given geometry. The three tests consisted of a kinetic (a.k.a. sliding) test, a stick-slip test, and a proof-of-concept test. The kinetic and stick-slip tests were performed with the same hemispherical samples made of the TangoPlus and VeroWhite materials while the proof-of-concept tests were made with the footpad design used for the SQUISHbot project, consisting of a composite of TangoPlus and VeroWhite materials.

3.2.1 Kinetic

Kinetic tests were performed at set rotation speeds ranging from 0.1 to 1 rad/s. For each test, the normal force applied to the sample was varied from 0.1 to 1 N while the rotation speed remained constant. Screenshots were used to capture the exact measured torque for a given normal force.

When loaded in the rheometer and subjected to the kinetic sliding test, the frictional force experienced by the hemispherical samples was linearly related to the applied normal force. This coincides with coulomb friction laws, and from the linear fit slope, the coefficient of kinetic friction can be found for the materials. Under sliding conditions, the required time to form an adhesive bond between the surface and sample materials is not achieved and therefore does not contribute to the torque recorded by the rheometer. Figure 19 shows a 3D printed sample loaded onto the 40 mm aluminum fixture on the rheometer
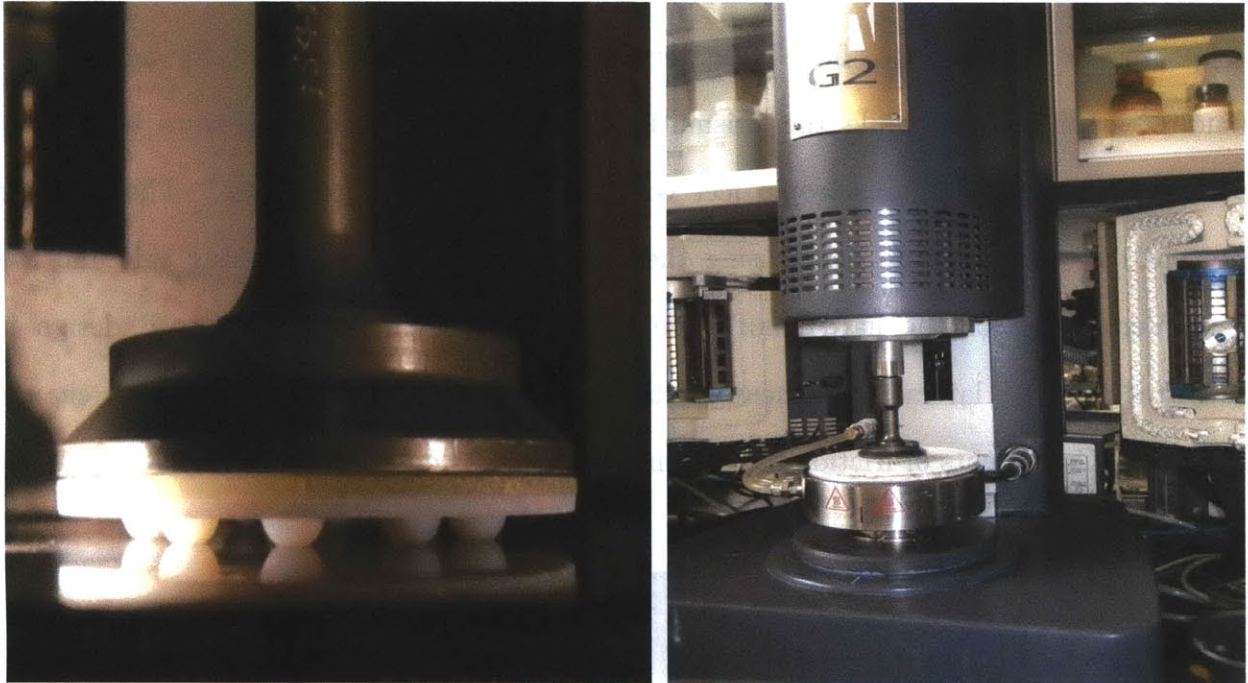
Figure 19: 3D printed sample loaded onto 40 mm aluminum geometry on the rheometer and the AR-G2 rheometer loaded with 3D printed sample on 40mm flat plate geometry.

3.2.2 Stick-Slip

For the static stick/slip tests, a monotonically increasing force was applied to the samples for a given normal force. Tests were performed under normal forces ranging from .1 to 1 N. For each test, the samples start off stationary (no angular velocity). A ramp procedure was applied until the force experienced by the samples transitioned to kinetic friction, at which point the samples would slip and the rheometer would experience an "overspin" error. The overspin error was the result of the abrupt change in resistive torque experienced by the machine, causing the geometery to spin very quickly. The applied torque ranged from 1000 UNIT to 15,000 UNIT for each sample.

3.2.3 Proof of Concept

In an attempt to find a material that allows SQUISHbot to move in a unidirectional manner while the prismatic joint is in use, numerous tests have been performed on different anisotropic feet configurations in the rheometer. The proof of concept test samples were made using the soft TangoPlus for the sticking side and the hard VeroWhite for the hard "nail" side. The functionality of the footpad design is activated by the lateral movement of the robot, which causes the pads to change direction. Coefficients of friction have been calculated for different feet designs.
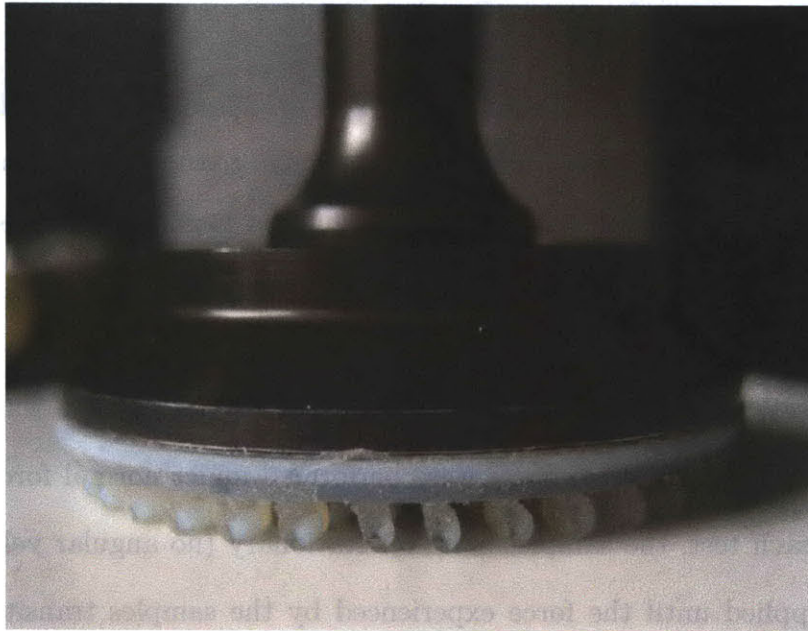

Figure 20: Proof of concept samples loaded on the 40 mm plate on the rheometer.

3.3 Results

Figure 21 shows the kinetic friction force plotted against the applied normal force per sphere for the 3D printed samples made of TangoPlus and FullCure720.

Kinetic Friction vs Normal Force per sphere

- ■ Hard Material (Fulcure720)
- ● Soft Material (TangoPlus)
- — Linear Fit of Soft Material (TangoPlus)
- — Linear Fit of Hard Material (Fulcure720)

$y = 0.405x - 0.000$

$y = 0.162x + 3E-05$

X-axis: Normal force per sphere (N)
Y-axis: Friction force per sphere (N)
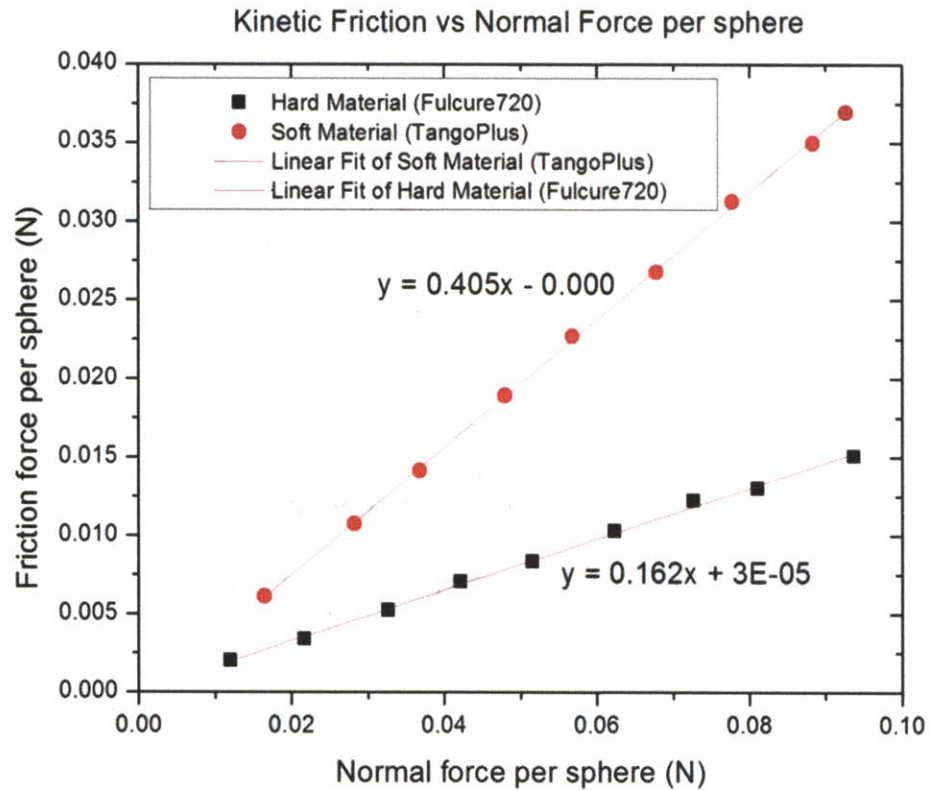
Figure 21: Kinetic friction vs. normal force per sphere for 3D printed samples with varying materials.

Figure 22 shows the friction force per sphere vs the applied normal force for the two types of materials used (TangoPlus and Fullcure720) during the two different tests (kinetic and stick-slip).
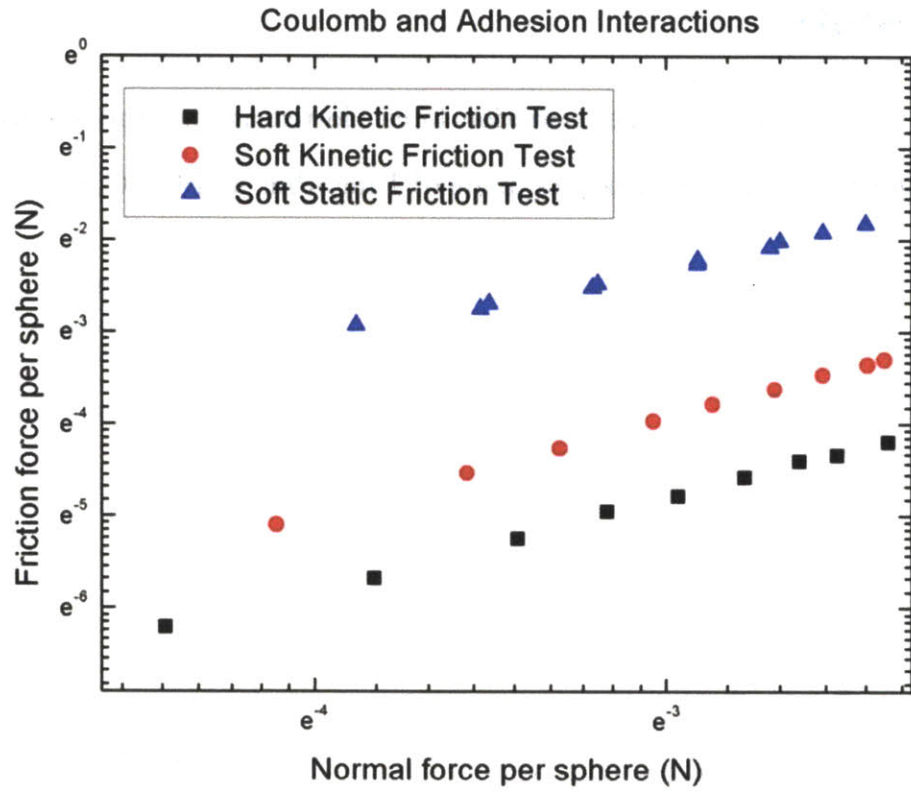
Figure 22: Friction force per sphere vs. applied normal force.

Figure 23 shows the results from the kinetic and stick-slip tests combined and scaled onto the same plot.
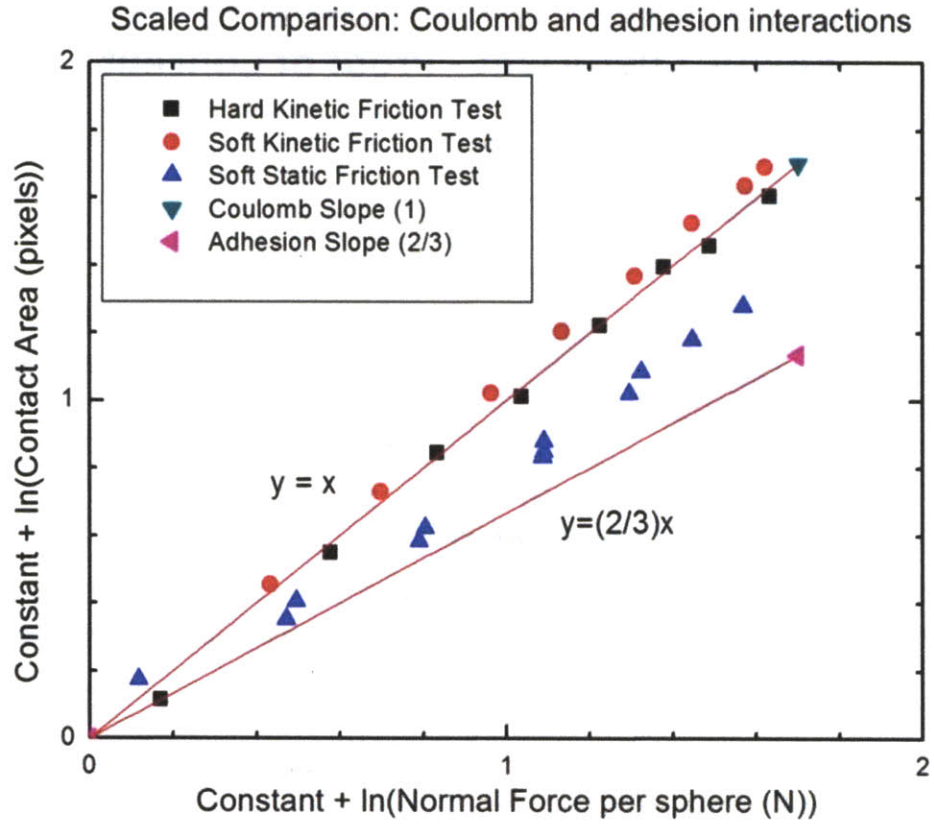
Figure 23: Results from kinetic and stick-slip tests combined and scaled on the same plot.

Figure 24 shows the kinetic coefficient results from the proof of concept samples that were used on the rheometer.

Figure 24: Kinetic coefficient results from proof of concept tests on the rheometer.

Figure 25 shows the kinetic coefficient results from the proof of concept samples that were used on the rheometer.

Figure 25: Static coefficient results from proof of concept tests on the rheometer.

3.4 Summary

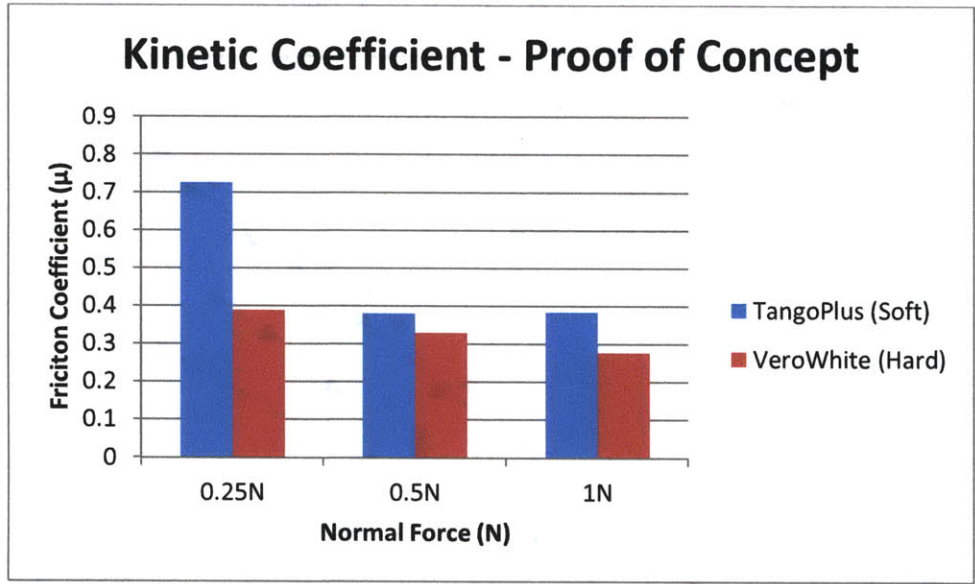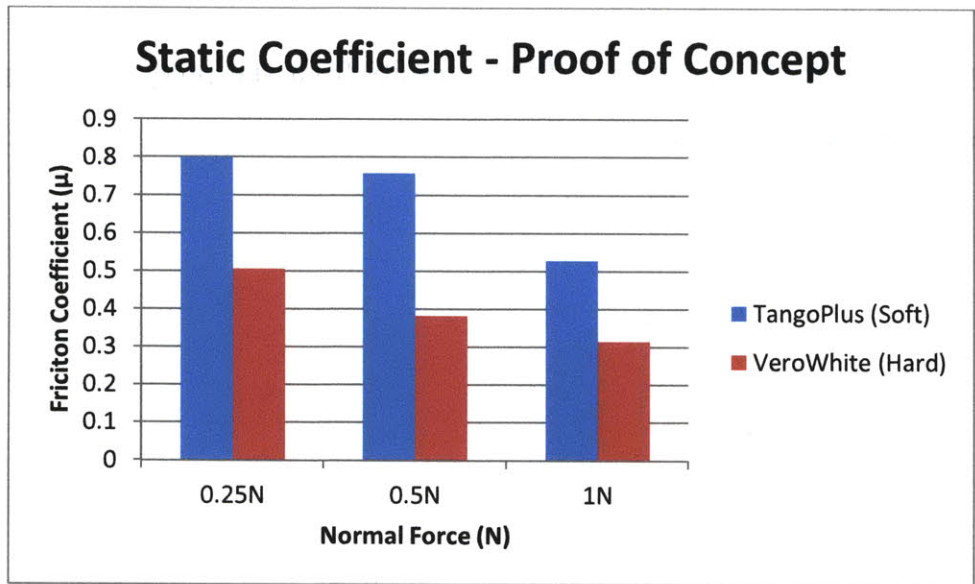When loaded in the rheometer and subjected to the kinetic sliding test, the frictional force experienced by the hemispherical samples was linearly related to the applied normal force (see Figure 21). This coincides with coulomb friction laws, and from the linear fit slope the coefficient of kinetic friction can be found for the materials. Under sliding conditions, the required time to form an adhesive bond between the surface and sample materials is not achieved and therefore does not contribute to the torque recorded by the rheometer.

For the stick-slip tests of the two materials loaded in the rheometer, two very different results could be seen. The FullCure720 samples experienced a frictional force that was again linearly related to the applied normal force. For the TangoPlus, however, the stick-slip tests showed that there was a power law relationship that was between 1 and 2/3. As expected, the softer TangoPlus material experienced higher friction loads in comparison to the hard FullCure720 for a given applied normal force. An increased frictional force was experienced during the stick-slip test for the TangoPlus samples in comparison to the sliding tests. This coincides with the added attractive adhesive bond between the surface and sample material. The results from Figure 22 were later scaled so that all plots started at the origin on Figure **23**. This allowed for a clear visual interpretation of the power law relations for each tests. For the kinetic tests, it can be seen that the samples experienced a frictional force that was linearly related to the applied normal force, which agrees with Coulomb's friction law. For the stick slip tests, however, it can be seen that all frictional force was between Coulomb's law and the 2/3$^{\text{rd}}$ power law expected for Hertzian contact contributions. This seems reasonable as adhesive forces would contribute to the frictional forces experienced prior to the samples transitioning to the slip regime. Figure 23 shows the combined plots with the applied

scaling. Chapter 4 takes an in-depth look into the area dependence for the TangoPlus material with respect do varying applied loads.

The proof of concept results clearly indicated that the softer TangoPlus produced a much higher coefficient of friction in comparison to the hard Fulcure720 material. For the kinetic proof of concept results, it can be seen that at the higher applied normal forces the coefficient of friction for the tango plus is greatly reduced. While sliding the material at the higher loads, the material was unable to remain intact and started to break apart. The shedding of material is most likely the cause for the reduced friction coefficient. The stick-slip tests produced higher coefficients of friction in comparison to the kinetic tests, which shows how the increased time of stationary contact increased the surface interaction between the materials.

4

VERIFICATION OF AREA DEPENDENCIES FOR ADHESIVES

As described in chapter 3, it is necessary to outline the effects of contact area interactions for soft materials in order to explain the change in scaling for the friction results. The change in contact area was measured under varying applied loads for the same samples used in the friction tests. MATLAB image processing was combined with photos depicting contact area for given applied loads to autonomously find the contact area. Results were found to be in agreement with the JKR theory described in chapter two and were also useful in describing the power relations experienced by the samples in the stick-slip tests outlined in chapter three.

4.1 Materials

The samples tested were made of the same TangoPlus used in the friction tests and were of the same geometries. To create the 3D printed samples, the same method was used as described in Section 3.1. The samples were imaged under varying applied normal forces using a Nikon Eclipse TE2000-S inverted microscope. The normal forces were applied to the center of the samples using a calibration mass set ranging from .2 to 100g. An MV BlueFox USB 2.0 CMOS camera with a resolution of 1600 x 1200 pixels was used

to image the contact surface of a single hemisphere. All photos were saved in the portable network graphics format (PNG). MATLAB code was then written to import the photos to be processed using MATLAB's image processing toolbox. Figure 26 shows a side view of the sample setup:
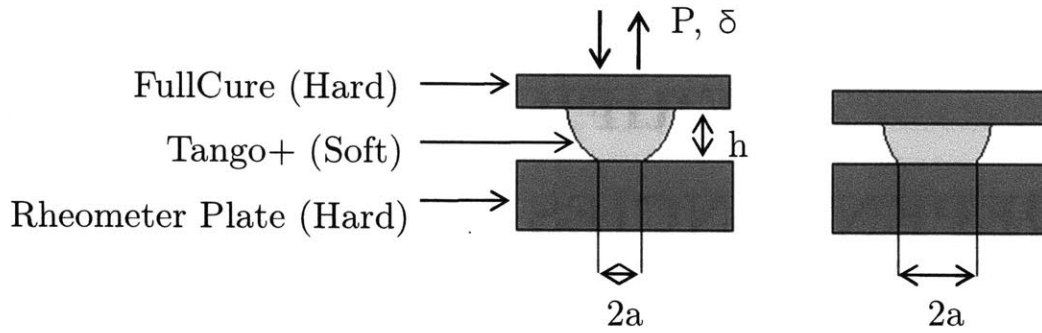

Figure 26: Illustration of the general setup for hemispherical compression tests.

4.2 Compression Test

The code first converted the image of the contact area to black and white using the im2bw command with a conversion level chosen to match that of the visible contact area. All objects containing fewer than 5000 pixels were automatically removed using the bwareaopen command so that only the area of the contacted material would be measured. Any holes created by abnormalities within the contact area were then filled in with the imfill command. The contact area of the sphere could then be found by finding the number of pixels contained within the white space for each image. Figure **27** shows an example of a compressed sample captured with the BlueFox camera and processed by MATLAB:
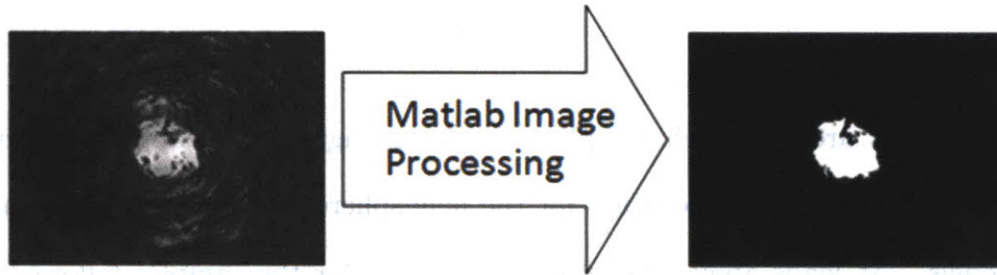
Figure 27: Matlab processing of compressed sample - converted to black & white image for area analysis.

4.3 Results

Figure 28 shows a plot of the contact area vs. the applied mass for the compression tests. The data was obtained from three different 3D printed samples made during different print times in the Objet 3D printer's maintenance cycle.
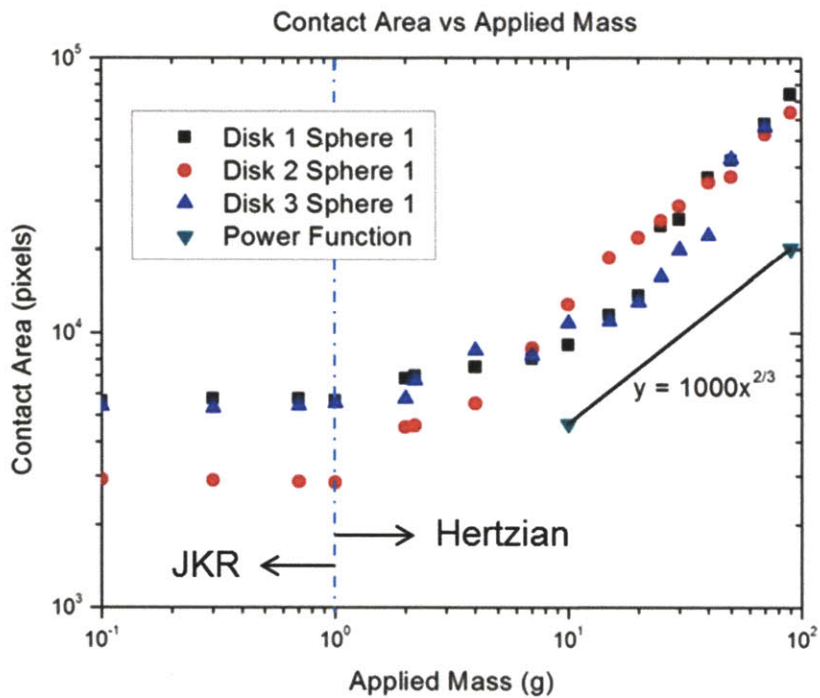
Figure 28: Plot of Contact Area vs Applied Mass for hemispherical compression tests.

4.4 Summary

The contact area for each sample was plotted against the applied normal force. Under compression, the area of contact for the hemispheres is in agreement with existing contact models. At loads above 10g, the contact area for the samples followed a power law that matched the theoretical Hertzian contact prediction as seen in Figure 28. At these higher loads, the effects of adhesion are less noticeable. At lower normal loads, the area of contact appears to remain constant, which coincides with adhesion prediction of the JKR theory.

5

BRISTLEBOT TESTING

The effects of varying surface roughness were studied for a given anisotropic arrangement of bristles. The array of bristles was used to provide propulsion to a controllable robot called BristleBot. The untethered nature of the robot allowed for unhindered velocity and force measurements that were used to analyze the effects of surface roughness. The force input for the robot was provided by two vibration motors that created an excitation which was then translated to horizontal movement by the anisotropic formation of the bristles. It was found that the BristleBot was able to achieve optimal locomotion when roughness conditions were minimized

5.1 Materials

The original BristleBot was a tiny directional vibrobot designed by Evil Mad Scientist Laboratory. It consisted of a toothbrush head, a watch battery, and a vibration motor. The BristleBot was intended to be a novelty toy that would move around in random directions on a table due to the motor vibrations. Figure 29 shows a BristleBot from EvilMadScientist.com [26].
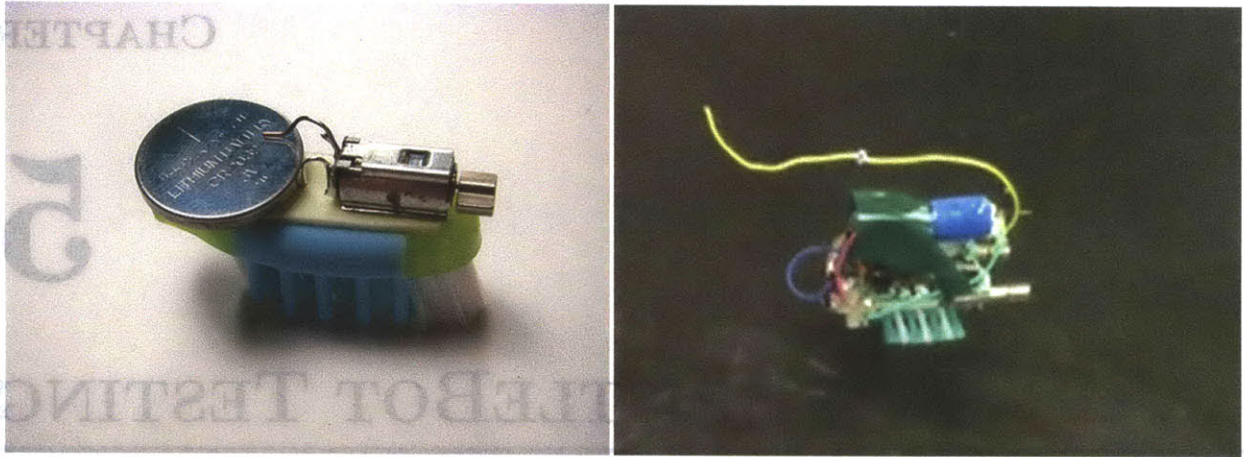
Figure 29: (Left) Evil Mad Scientist BristleBot and (Right) University of Maryland BristleBot designs. Images reproduced from [26] and [27].

An adaptation to this was developed by a senior project at the University of Maryland, where two vibration motors were attached to the toothbrush head [27]. An RC board was attached so that the motors could be independently controlled. With the motors on either side of the bristle head, as one vibration motor moved the bristles some of the bristles on the head were vibrated more than others, resulting in a directional movement that could be used to the steer the robot.

The BristleBot design used for this thesis consisted of two toothbrush heads that are angled towards each other. The toothbrush heads were modified so that all of the bristles were angled in the same direction to achieve maximum anisotropy. The vibration motors were attached to the back of each toothbrush head. When one vibration motor was activated, the corresponding toothbrush head vibrated while the other head remained stationary, thus causing the BristleBot to move forward and turn. When both vibration motors were activated, the opposing turning forces were canceled out and the robot moved in a straight line forward.
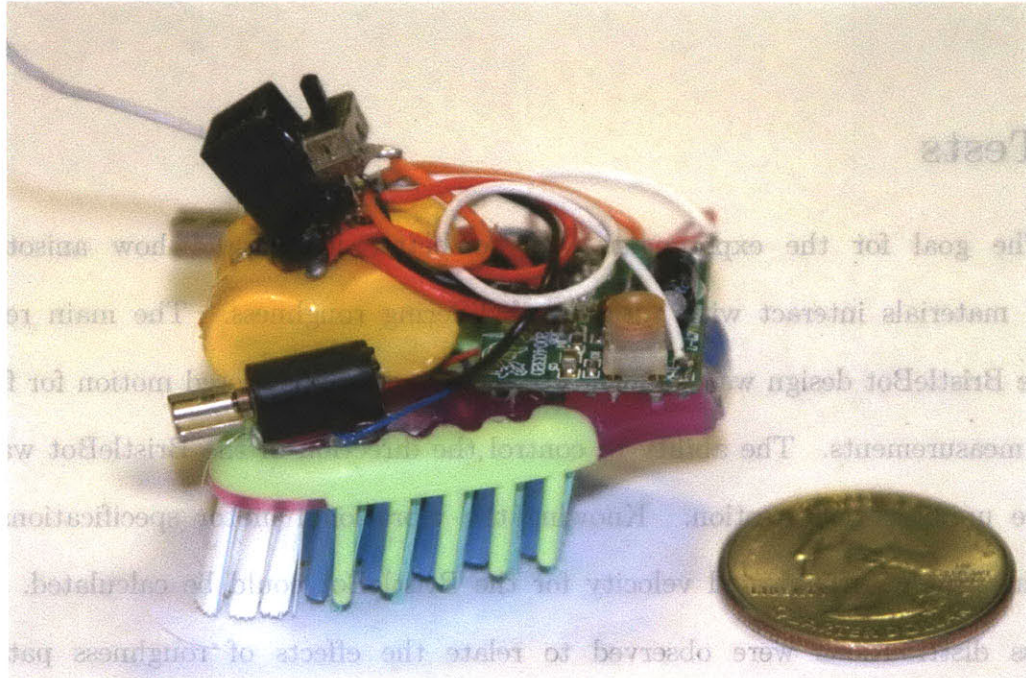
Figure 30: Final BristleBot Design used in velocity and surface testing.

The vibration motors were independently controlled by a 27mHz RC board. The board came from a toy boat that had two propellers that could be independently controlled to move the boat forward, backwards, or turn. The remote control, rechargeable battery, on/off switch, antenna, and charging port also came from the same toy boat.
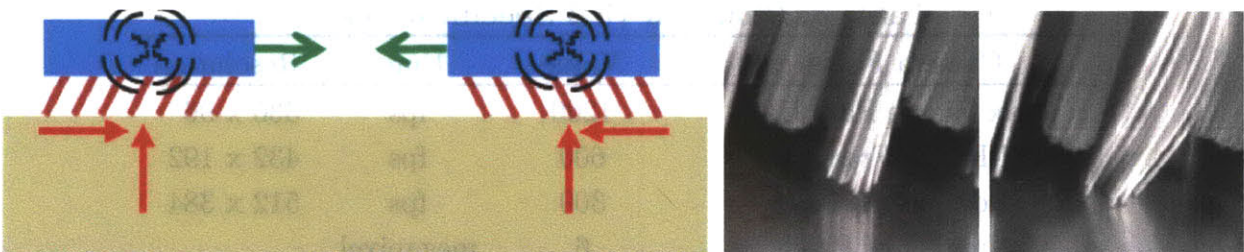

Figure 31: (Left) Sketch illustrating influence of microstructure geometry in simple "bristle" locomotion, also known as "ciliary vibration." (Right) Two high-speed images showing the bristle dynamics as the platform locomotes.

5.2 Tests

The goal for the experiments was to better understand how anisotropically designed materials interact with surfaces of differing roughness. The main reason for using the BristleBot design was to achieve tetherless and unhindered motion for force and velocity measurements. The ability to control the direction of the BristleBot was added to ensure unidirectional motion. Knowing the vibrational motor specifications, power input, and weight an expected velocity for the BristleBot could be calculated. Surface roughness distributions were observed to relate the effects of roughness patterns to velocity performance.

5.2.1 Velocity

High-speed imaging was used to film the surface-bristle interaction as well as to calculate the velocity of the BristleBot on various surfaces. Two different high-speed cameras were used:

Table 4: Phantom v5.2 Specifications

Camera Feature	Value	Units	Resolution
Max Frame Rate Used	1200	fps	336 x 96
Mid-Range Frame Rate	600	fps	432 x 192
Low Frame Rate	300	fps	512 x 384
Number of Pixels	6	megapixel	
Image Sensor	1/1.8 inch hs CMOS		

Table 5: Casio EX-F1 Specifications

Camera Feature	Value	Units	Resolution
Max Frame Rate Used	10362	fps	256 x 256
Low Frame Rate	1000	fps	1152 x 896
Number of Pixels	1	megapixel	
Minimum Exposure Time	2	μs	
Sensor ISO	2400	monochrome	

Table 6: BristleBot Specifications

Bot Property	Value	Units
Average Velocity	0.2	m/s
Maximum Velocity	0.3	m/s
Average Bristle Jump Height	0.077	mm
Power Consumption	0.618	W
Total Bot Mass	23.21	g
Motor Balance Mass	1.9	g
Motor Balance Radius	1.7	mm

Estimated values for the expected BristleBot speeds and heights were found through analysis of the motor input and the physical constraints of how the bot moved. First, the input force from the vibration motors was calculated using the centripetal force:

$$F_m(t) = 2 * m_{motor} * \omega^2 r \sin(\omega t) \tag{7}$$

Where m_{motor} is the mass of the unbalanced weight on the motor, r is the radius of rotation for the mass, and ω is the angular velocity of the weight. The force input was then integrated over the time that the bristles were in contact with the traversed surface per revolution of the unbalanced weight:

$$\mathbf{v_x} = \mathbf{u_0} + \int_0^{.00475s} \frac{\mu F_{motor}(t)}{m_{bot}} dt \tag{8}$$

Where v_x is the velocity of the bot, u_o is the initial velocity, m_{bot} is the mass of the bot, and μ is the coefficient of friction.

$$\mathbf{v_y} = \frac{1}{m_{bot}} \int_0^{.00475s} m_{motor} \omega^2 r(\sin(\omega t) + 1) dt \tag{9}$$

Efficiency calculations for the BristleBot were found using the following equations:

$$\eta = \frac{want}{cost} \tag{10}$$

$$\eta_{bristlebot} = \frac{v_{avg} * m_{bot}}{PowerConsumption} \tag{11}$$

Where η is the total efficiency, and v_{avg} is the average bot velocity.

Velocity tests were performed on thirteen different surfaces with varying roughness. The roughness of the surfaces was measured using Mitutoyo's Surftest SJ-210. To find the BristleBot's velocity on each different surface, high-speed video of the bot moving in a straight line was shot at 600 frames per second. The distance traveled over a given number of frames by the bot was measured in the video and later converted to a horizontal velocity.

5.2.2 Trajectory

High-speed video was taken of the BristleBot's body platform while in motion to find the recoil height of the bot while in motion. The bot's bounce height was calculated by recording the pixel location of markers drawn on the bot's body in each high-speed video frame. The change in pixel location for each marker was then converted to a distance measurement.
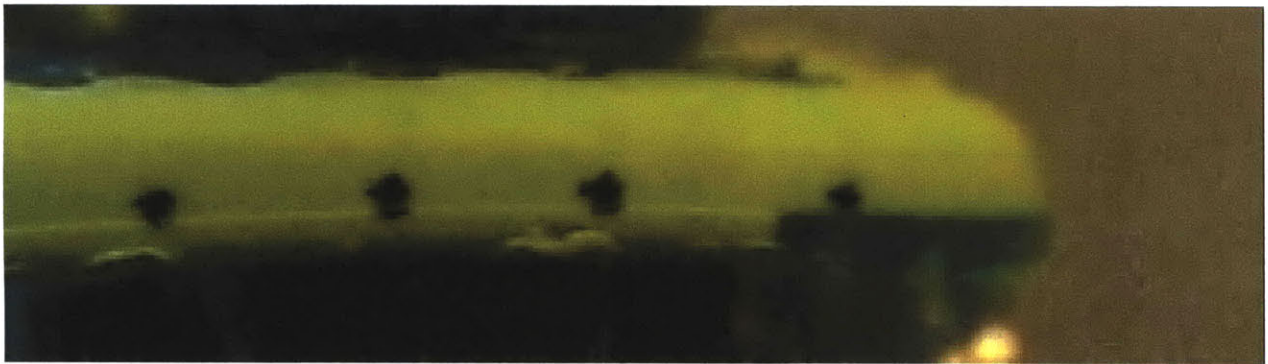

Figure 32: Image from high speed video used to monitor "bounce" position for points on BristleBot body.

5.3 Results

Figure 33 shows a plot of the BristleBot's velocity for varying surfaces with different roughnesses
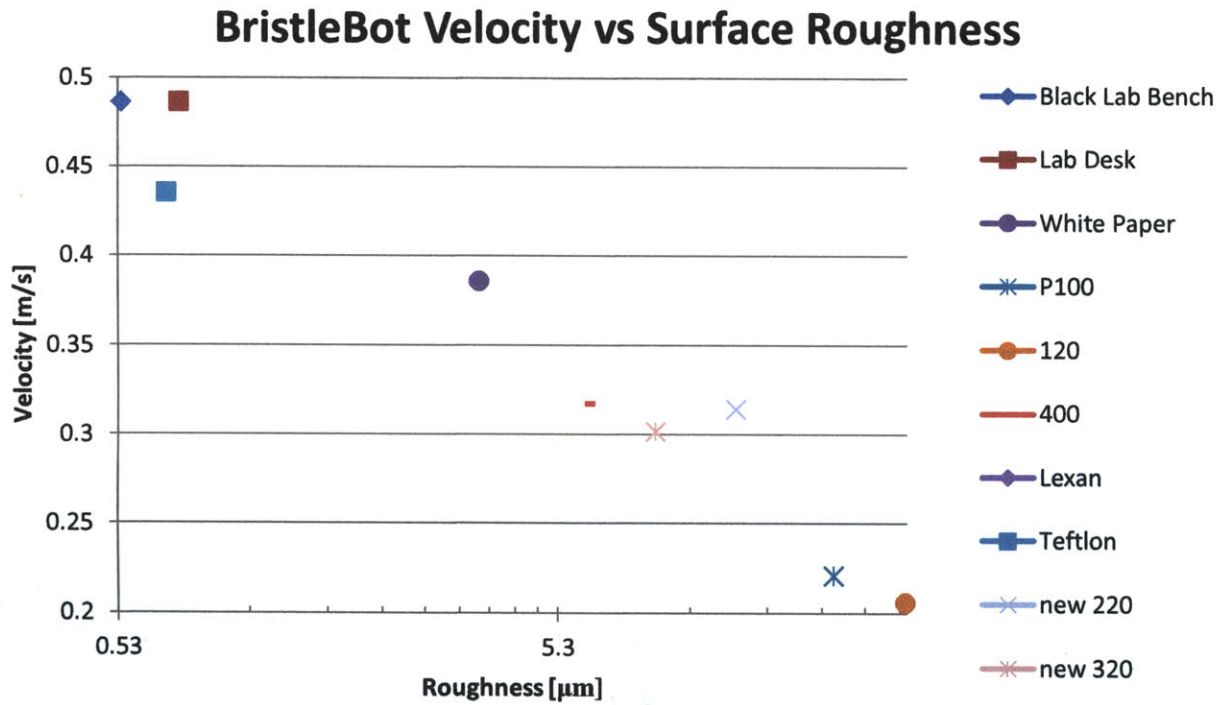
Figure 33: BristleBot Velocity for varying surface roughness interactions.

Figure 34 shows the "bounce" profile for a given point on BristleBot's body over a given traveled distance. The black dot furthest to the right in Figure 32 was used for the measurements.
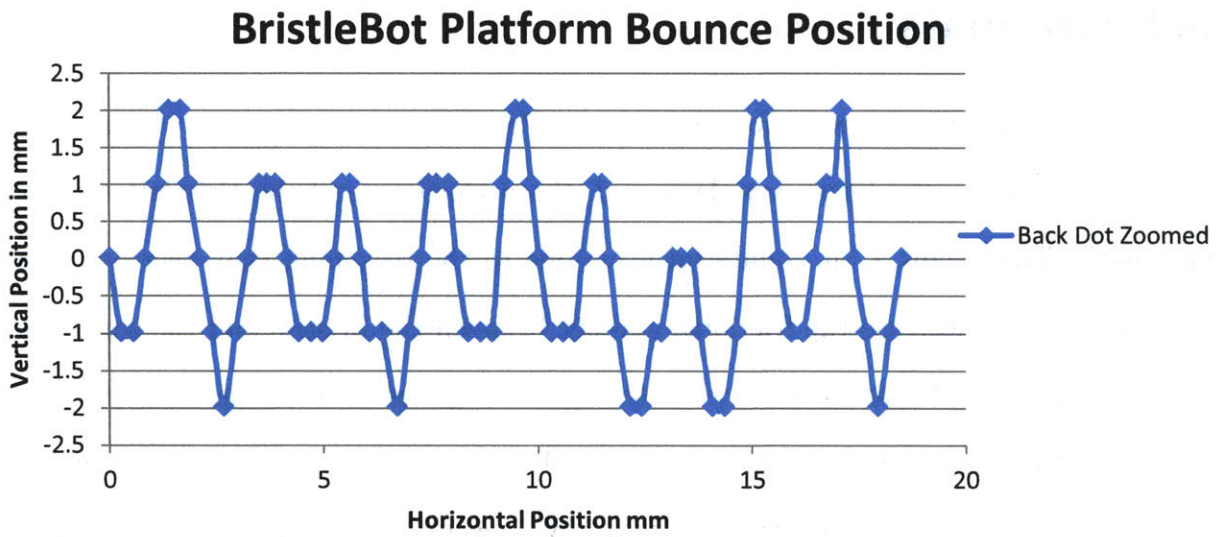
Figure 34: "Bounce" profile for a given point on BristleBot body over a traveled distance.
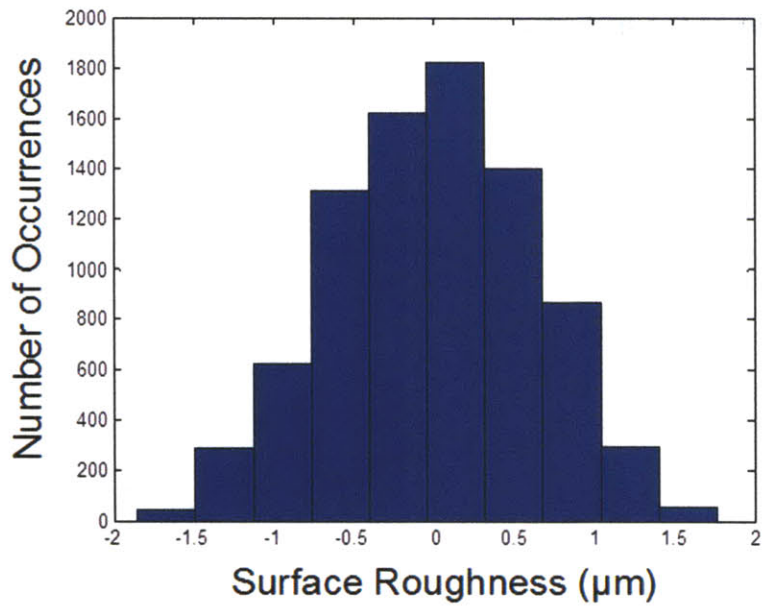

Figure 35: Surface roughness distribution for white paper.

5.4 Summary

Interesting results were found from the BristleBot velocity tests. It can be seen that as the surface roughness was decreased, the performance of the BristleBot's velocity increased. This seems a bit counterintuitive due to the reasoning that decreased surface roughness would decrease the frictional contact between the bristles and the surface itself. It can be speculated that for surfaces with higher roughness, the inclusions in the surface were actually more of a hindrance to the Bristles and acted as a form of barriers to the bot's movement, creating resistive friction. We speculate that the logarithmic relation between the BristleBot's velocity and surface roughness can be related to the Gaussian distribution of the surface roughness as seen in Figure 35. The probability of the bristles being able to "jump" out of a given inclusion is dependent on the BristleBot's jump height and the actual height of the inclusion.

6

CONCLUSIONS

We have gained a better understanding of the design, fabrication, and mechanical optimization for multi-scale anisotropic feet though friction, adhesion, and BristleBot tests. Laws of coulomb friction were proven to hold for the 3D printed samples with high moduli of elasticity, while the frictional results for the softer samples were related to the adhesive effects associated with increased contact area. Hertzian contact laws were also shown to hold true for the 3D printed samples. The compression test results were in accordance with prior contact theories as described by Johnson, Kendall, and Roberts. The effects of varying surface terrain have also become better understood for anisotropically aligned bristles and theories have been made as to how surface roughness effects force transmission.

6.1 Future Work

There are many opportunities for advancements in the field of multi-scale robotic development. Combining locomotion methods is one of the best methods of achieving locomotion over a wide range of surface variants. There have been promising results involving the use of magnetorheological fluid as a switchable adhesive, which could be combined with other locomotion methods to allow for vertical and even inverted-body propulsion methods. Other work has initiated which focuses on varying the properties of

the anisotropically aligned bristles through geometric and material adaptations. Such adaptations include changes in length, radii, and beam stiffness of the bristles to allow for improved movement over different surface inclusions. The ability to freely move in multiple directions through anisotropic material and geometry designs is also being studied. Omni-directional traversing methods have been shown to greatly increase the maneuverability of robots

REFERENCES

[1]   K. Kendall, "Adhesion: molecules and mechanics.," *Science (New York, N.Y.)*, vol. 263, 1994, pp. 1720-5.

[2]   J. Carlson and R. Murphy, "How UGVs physically fail in the field," *IEEE Transactions on Robotics*, vol. 21, 2005, pp. 423-437.

[3]   K.J. Dowling, A. William, and L. Whittaker, *Limbless locomotion: learning to crawl*, 1999.

[4]   S. Kim, M. Spenko, S. Trujillo, B. Heyneman, V. Mattoli, and M.R. Cutkosky, "Whole body adhesion: hierarchical, directional and distributed control of adhesive forces for a climbing robot," *Proceedings 2007 IEEE International Conference on Robotics and Automation*, 2007, pp. 1268-1273.

[5]   *Defense Sciences Research and Technology Secial Focus*, Defense Sciences Office, 2008.

[6]   K. Hatazaki, M. Konyo, K. Isaki, S. Tadokoro, and F. Takemura, "Active scope camera for urban search and rescue," *2007 IEEE/RSJ International Conference on Intelligent Robots and Systems*, 2007, pp. 2596-2602.

[7]   *Introduction to Tribology – Friction*, Washington: University of Washington, 2003.

[8]   B.N. Persson, *Sliding friction: Physical principles and applications*, Berlin: Springer-Verlag, 1998.

[9]   B. Townsend, *Static and Kinetic Friction*, 2002.

[10]   J. DiMarco, *Area Dependence of Friction*, University of Montana, .

[11]   Y. Mo, *Friction Laws at the Nanoscale*, Computational Materials Group, 2006.

[12]   M.K. Chaudhury and G.M. Whitesides, "Direct measurement of interfacial interactions between semispherical lenses and flat sheets of poly(dimethylsiloxane) and their chemical derivatives," *Langmuir*, vol. 7, 1991, pp. 1013-1025.

[13]   N. Maeda, N. Chen, M. Tirrell, and J.N. Israelachvili, "Adhesion and friction mechanisms of polymer-on-polymer surfaces.," *Science (New York, N.Y.)*, vol. 297, 2002, pp. 379-82.

[14]   J.a. Greenwood and J.B. Williamson, "Contact of Nominally Flat Surfaces," *Proceedings of the Royal Society A: Mathematical, Physical and Engineering Sciences*, vol. 295, 1966, p. 300–319.

[15]   J. Greenwood, "Analysis of elliptical Hertzian contacts," *Tribology International*, vol. 30, 1997, p. 235–237.

[16]   K.L. Johnson, K. Kendall, and A.D. Roberts, "Surface Energy and the Contact of Elastic Solids," *Proceedings of the Royal Society of London. Series A, Mathematical and Physical Sciences*, vol. 324, pp. 301-313.

[17]   G. Cyprien and L. Ludwik, "On Stickiness," *Physics Today*, vol. 52, 1999, pp. 48-52.

[18]   J.F. Waters and P.R. Guduru, "Mode-mixity-dependent adhesive contact of a sphere on a plane surface," *Proceedings of the Royal Society A: Mathematical, Physical and Engineering Science*, vol. 466, pp. 1303-1325.

[19]   J.F. Waters and P.R. Guduru, "Mode-mixity-dependent adhesive contact of a sphere on a plane surface," *Proceedings of the Royal Society A: Mathematical, Physical and Engineering Science*, vol. 466, pp. 1303-1325.

[20]   M.K. Chaudhury and G.M. Whitesides, "Direct measurement of interfacial interactions between semispherical lenses and flat sheets of poly(dimethylsiloxane) and their chemical derivatives," *Langmuir*, vol. 7, 1991, pp. 1013-1025.

[21]   M. Barquins and A. Roberts, "Rubber friction variation with rate and temperature: some new observations," *Journal of Physics D: Applied Physics*, vol. 19, 1986, p. 547.

[22]   a.a. Koudine, M. Barquins, P.H. Anthoine, L. Aubert, and J.L. Lévêque, "Frictional properties of skin: proposal of a new approach.," *International journal of cosmetic science*, vol. 22, 2000, pp. 11-20.

[23]   B.N. Persson, "On the mechanism of adhesion in biological systems," *The Journal of Chemical Physics*, vol. 118, 2003, pp. 7614-7621.

[24]   D. Sameoto, Y. Li, and C. Menon, "Multi-Scale Compliant Foot Designs and Fabrication for Use with a Spider-Inspired Climbing Robot," *Journal of Bionic Engineering*, vol. 5, 2008, pp. 189-196.

[25]   A. Asbeck, S. Kim, A. McClung, A. Parness, and M. Cutkosky, "Climbing walls with microspines," *IEEE ICRA, May*, 2006.

[26]   W.H. Oskay, *Bristlebot: A tiny directional vibrobot*, 2007.

[27]   umdseniorproject, *Steerable Bristle Bot Attempts Maze*, 2008.

[28]   Zhermack, *Elite Double 8.*

A

MATLAB CODE FOR
COMPRESSION TESTS

```
clear
clc


area=zeros(18,2);
for i=1:1:18
filename=['d5b1' num2str(i) '.png'];
%Convert the image to black and white in order to prepare for boundary
%tracing using bwboundaries
I = imread(filename);
%Converts image I to black and white with level of .x conversion
bw = im2bw(I,.59);
% remove all object containing fewer than xxx pixels
bw = bwareaopen(bw,2500);
% fill any holes, so that regionprops can be used to estimate
% the area enclosed by each of the boundaries
bw = imfill(bw,'holes');
subplot(4,5,i)
imshow(bw,'border','tight')
%Outputs pixel area of white space
area(i,1)=i;
area(i,2)=bwarea(bw);
 end


x = [0,.1,.3,.7,1,2,2.2,4,7,10,15,20,25,30,40,50,70,90];
y = area(:,2);
z = area(10,2);
x1=[10,90];
y1=[10^(2/3),90^(2/3)];
```

```
figure
loglog(x,y)
hold on
loglog(x1,1000*y1)
xlabel('(log) applied mass (g)');
ylabel('(log) contact area (pixels)');
title('Disk 1 Ball 1 Contact Area vs Applied Mass');
```

B

ADDITIONAL SAMPLE CREATION

In addition to the 3D printed samples, a mold was created that allowed us to create samples to be made out of additional materials with properties that were different than those of the 3D printer materials. The mold was an inverse replica of the 3D printed version. The material used to fill the mold consisted of a soft silicon compound that is typically used for dental molds. The hard mold shell was created using Objet's Fullcure720. The silicon samples were fabricated using Zhermack's Elite Double 8 and made according to the manufacturer's instructions [28]. The material itself is polysiloxane. It is a very elastic material with a Young's Modulus of 1.2 MPa and a density of 1.4 g/cm³.
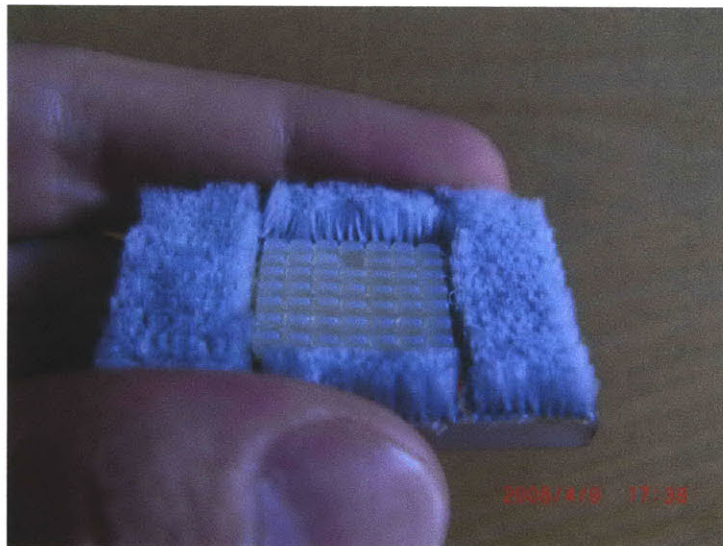

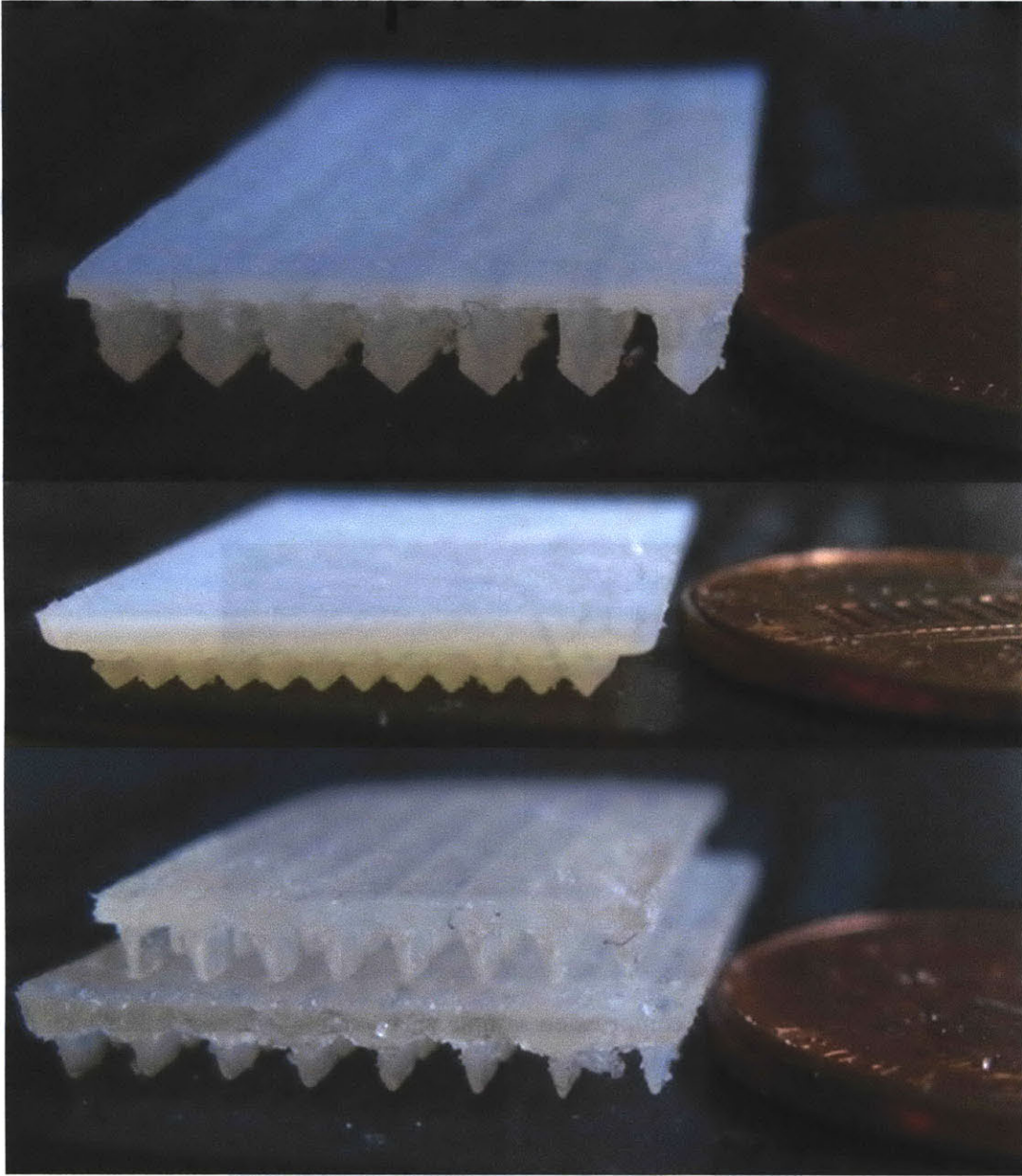Figure 36: 3D printed feet combined with anisotropic fibers.

Figure 37: Additional types of anisotropic feet designed for SQUISHbot testing.

C

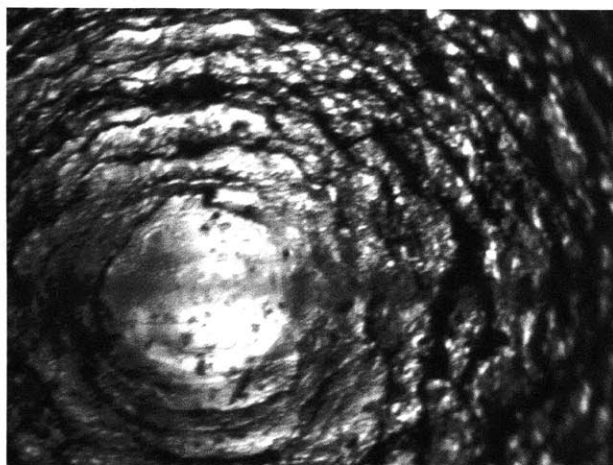# BlueFox Calibration Measurements

Figure 38: Microscope image of compression sample with sample focus for calibration length.
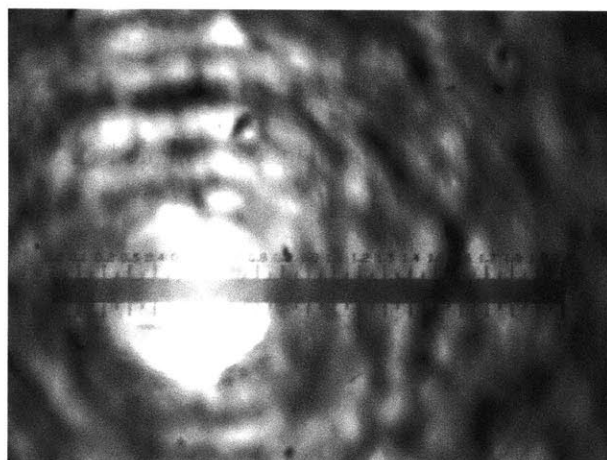

Figure 39: Microscope image of compression sample with measuring tape in focus for calibration length.